Spatial Dynamics in Yeast Galactose Switch Revealed Through RDME-ODE Hybrid 4D Simulation

Tianyu Wu[1,2], Marie-Christin Spindler[3,2], Emmy Earnest[4], Henry Li[2], Zane R. Thornburg[5,6], Julia Mahamid[3,7,2], Zaida Luthey-Schulten[8,2,1*]

1 Center for Biophysics and Quantitative Biology, University of Illinois at Urbana–Champaign, Urbana, IL, USA
2 National Science Foundation Science and Technology Center for Quantitative Cell Biology, Beckman Institute for Advanced Science and Technology, University of Illinois at Urbana–Champaign, Urbana, IL, USA
3 Molecular Systems Biology Unit, European Molecular Biology Laboratory (EMBL), Heidelberg, Germany
4 Department of Physics, University of Illinois at Urbana–Champaign, Urbana, IL, USA
5 Beckman Institute for Advanced Science and Technology, University of Illinois at Urbana-Champaign, Urbana, IL, USA
6 Cancer Center at Illinois, University of Illinois at Urbana-Champaign, Urbana, IL, USA
7 Cell Biology and Biophysics Unit, European Molecular Biology Laboratory (EMBL), Heidelberg, Germany
8 Department of Chemistry, University of Illinois at Urbana–Champaign, Urbana, IL, USA

* zan@illinois.edu

Abstract

We present the first 4D simulations of the galactose switch in *Saccharomyces cerevisiae* using a hybrid framework that integrates reaction diffusion master equations (RDMEs) and ordinary differential equations (ODEs). Using the GPU-based Lattice Microbes program, genetic information processes were simulated stochastically while a simplified metabolism was modeled deterministically. Cell geometry was constructed based on recently acquired cryo-electron tomograms, which allows us to quantify and differentiate between cytosolic ribosomes and endoplasmic reticulum(ER) associated ribosomes. This allows us to simulate realistic numbers of available ribosomes for ER-associated translation of proteins destined for the cell membrane, like the galactose transporter G2. Our simulations show that an extracellular 11 mM galactose triggers expression of 10k-15k galactose transporters within 60 minutes. We also benchmarked the multi-GPU solver's performance under various spatial decompositions. Our work underscores the challenges of whole cell modeling of eukaryotic cells and the effects of their inherent spatial heterogeneity.

Author summary

Cells must quickly adapt when their food source changes. In baker's yeast, a genetic switch turns on dozens of genes so the cell can use the sugar galactose instead of glucose. We built the first four-dimensional computer model that follows every key molecule in a realistic, tomogram-based yeast cell as this switch is involved. The model combines random, molecule-by-molecule chemistry for rare events with faster, deterministic equations for abundant reactions, and runs on graphics-processing units powerful enough to simulate an entire cell in an hour. By explicitly distinguishing ribosomes that float freely from those anchored on the endoplasmic reticulum, we tracked where the galactose transporter Gal2 is made and how it travels to the cell membrane. The simulations predict that about 10,000–15,000 transporters appear within an hour after the cell senses 11 mM galactose, and reveal that the maze-like endoplasmic reticulum slows their delivery. Our framework shows how cellular geography alters genetic information processing production and paves the way for whole-cell simulations of more complex organisms.

Introduction 1

The yeast galactose switch in the budding yeast *Saccharomyces cerevisiae* is a regulatory network controlling the expression of genes involved in the galactose metabolism in the absence of glucose as a preferred carbon source [1, 2]. This regulatory system comprises 39 molecular species and 75 biochemical reactions, integrated in three distinct feedback loops—two positive and one negative—that dynamically respond to changes in extra- and intra-cellular galactose concentration. As illustrated in Figure 1, the system involves five genes, G1-4 and G80 whose expression is induced when glucose is depleted and yeast switches to metabolizing galactose. Briefly, the activator G4d binds to the promoter region of the GAL genes excluding itself and initiates transcription. With galactose as the carbon source, the inducer G3 binds to intracellular galactose and forms a complex with the repressor G80d, facilitating the expression of the Gal genes. The protein G1 catalyzes the initial metabolic conversion of galactose into galactose-1-phosphate. Since our current model does not explicitly account for downstream metabolic pathways, it is represented at the moment as a dead-end in Figure 1. Protein G2 is the galactose transporter, which is translated at the ER and transported to cell membrane to mediate galactose uptake into the cell.

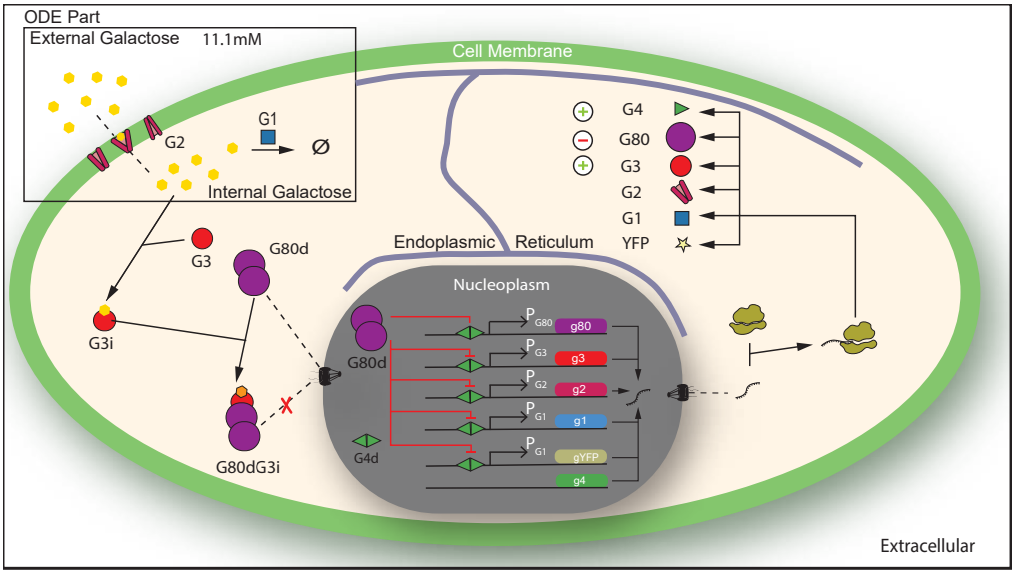

Fig 1. Schematic representation of the galactose switch model in budding yeast. The ODE reactions are depicted in the black box at the top left. G4d and G3 act as positive regulators, while G80d functions as a repressor. Here, the suffix "d" denotes the dimeric form of the protein.

This regulatory pathway was previously simulated as a well-stirred system by Bianchi *et al.* [3] and the yeast geometry was constructed by Earnest *et al.* [4]. However, the constructed model lacks the ER and does not distinguish between free cytosolic ribosomes and ER-associated ribosomes. It considers the simple case of a sugar-induced expression of a single gene and was simulated by spatially decomposing the yeast using the multi-GPU RDME solver in Lattice Microbes [5]. Meanwhile, we refine this model by introducing spatial complexity through a RDME-ODE hybrid approach, assigning reactions, diffusion coefficients and species to biologically relevant cellular compartments.

Hybrid RDME-ODE approaches partition reactions into two subsets: those involving fast reactions or highly abundant species are approximated deterministically using ODEs, while reactions involving low-copy species or high stochasticity are retained within the stochastic framework. Specifically, we modeled reactions involving

low-abundance species that exhibit high stochastic variability—such as transcription, translation, and regulator- promoter interactions—using Gillispie's stochastic simulation algorithm RDME [6]. Conversely, reactions characterized by large particle numbers or high reaction rates, including galactose transport and metabolism, were represented deterministically with ODEs. Spatial heterogeneity was explicitly incorporated by partitioning the cellular geometry into distinct compartments of the cell membrane, cytoplasm, nucleus, mitochondria, vacuole, and ER, each governed by RDME kinetics, thereby facilitating diffusion-driven interactions among neighboring subregions. Compared with previous works, the current model includes the previously missing ER and distinguishes between free ribosomes and ribosomes associated with the ER. We quantified the number of ribosomes translating into the ER directly from cryo-ET of wildtype *S. cerevisiae* cells. Our spatially resolved hybrid RDME-ODE approach enables the integration of molecular heterogeneity with reaction-diffusion dynamics, providing a more biologically realistic representation of subcellular processes.

Here, we model gene expression, regulation and transcription within the nucleus, while translation is simulated either at cytoplasmic ribosomes or ER-associated ribosomes. Transcriptional regulators (G4d and G80d) and mRNAs, diffuse through nuclear pore complexes in our model, while the transporter protein G2 is translated at the ER and then diffuses through its lumen to be integrated into the cell membrane.

Simulations were conducted under physiologically relevant conditions, including an extracellular galactose concentration of 11.1 mM (0.2% w/v) [1]. We validated the system's regulatory dynamics through the analysis of key species involved in transcriptional control. To assess spatial effects, we compared the outcomes of our RDME-ODE hybrid model with the previously published well-stirred CME-ODE model [3]. We next investigated the functional role of the ER in the trafficking of membrane-bound G2, demonstrating that ER architecture significantly delays G2 delivery to the cell membrane. We further examined the impact of reduced ER-bound ribosome density on translational dynamics. Finally, we evaluated how variations in ribosome abundance influence the system behavior by explicitly modeling the fraction of ribosomes actively engaged in translation. [7, 8] With optimized multi-GPU solver running on Nvidia A100 and H100, the performance is dramatically improved. By demonstrating the critical influence of spatial organization on genetic regulatory networks, our work underscores the importance of incorporating spatial heterogeneity in computational models of cellular processes in yeast and beyond.

Materials and methods

65

0.1 Geometry Reconstruction from Cryo-ET

The 3D geometry of budding yeast *Saccharomyces cerevisiae* cells was reconstructed using cryo-ET data acquired from vitrified yeast samples prepared via cryo-focused ion beam (cryo-FIB) milling. Detailed information of the data used here was reported in Earnest et al. [4]. Briefly, tomographic volume of approximately $2.04 \times 1.91 \times 0.242$ μm^3 at a pixel size of 5.31 Å, were reconstructed using the IMOD tomography package [9]. Due to the limited field of view, missing structures outside the tomographic volume were extrapolated based on known volumetric and structural constraints (described below). The reconstructed geometry was downsampled to a lattice resolution of 28.67 nm to balance simulation accuracy and computational efficiency.

0.1.1 Extrapolation of Missing Geometries

The extrapolation of missing or incomplete geometries was performed by fitting ellipsoidal models to the segmented tomographic data. The partial nuclear envelope and plasma membrane were initially represented as binary masks derived from segmentation as in Fig 2(a). To construct an ellipsoidal structure, nine parameters are required: three for radii, three for rotational angles, and three for the center coordinates of the ellipsoid.

To represent the cytoplasm, cytoplasmic membrane, nucleoplasm, and nuclear envelope, we used partial geometric data from the tomogram and applied the `scipy.optimize.minimize` function to fit ellipsoidal masks onto the existing structures. The ellipsoidal fitting process followed the methodology described in Earnest et al. [4]. We further implemented 139 nuclear pores extrapolated based on the nuclear pore density (nuclear pores are represented as white cross on the nuclear envelope as in Fig 2(c))

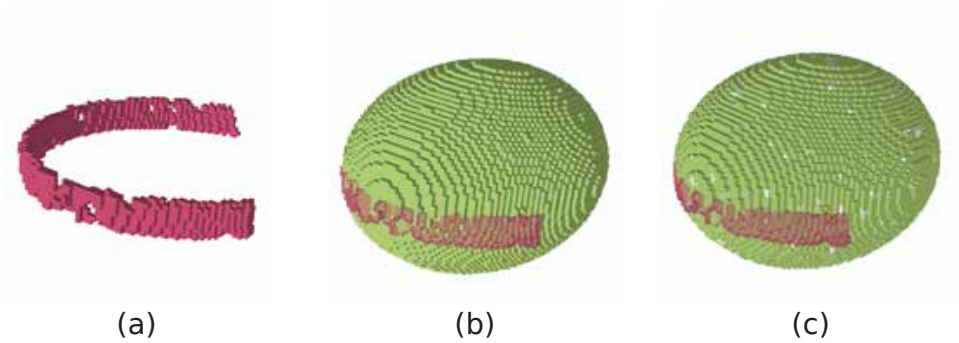

Fig 2. Geometric reconstruction of the nuclear envelope.(a) Segmented slice from cryo-electron tomography (cryo-ET) data.(b) Ellipsoidal fitting of the nuclear envelope.(c) Addition of nuclear pore complexes as white crosses to the reconstructed envelope.

0.1.2 Mitochondria, Vacuole, and Cell Wall

The cryo-ET volume only contains a fraction of the mitochondrial network, vacuoles, and the cell wall. We utilized the volumetric percentage of each organelle [10].

- **Cell Wall** was assumed to share the same rotational angles and center as the plasma membrane, and its radii were back-calculated based on the volumetric occupancy (15.9%).
- **Vacuole** occupy 0.75% of the total cell volume. Since budding yeast typically contains a single vacuole, its geometry was constrained to an ellipsoidal shape

with semi-major axes (a, b) randomly selected between 0.9 and 1.0, and the third radius $c = 1/(ab)$ to maintain the volume. Rotational angles are randomly determined to avoid the vacuole overlap with nucleus.

- **Mitochondria** occupy 0.16% of the total volume. Based on BioNumbers data ID:103068 [11, 12], there are approximately three mitochondria per yeast cell. The total mitochondrial volume was divided equally among these three compartments, with each ellipsoidal mitochondrion randomly placed within the cytoplasmic region using random orientations while ensuring no overlap with existing intracellular structures.

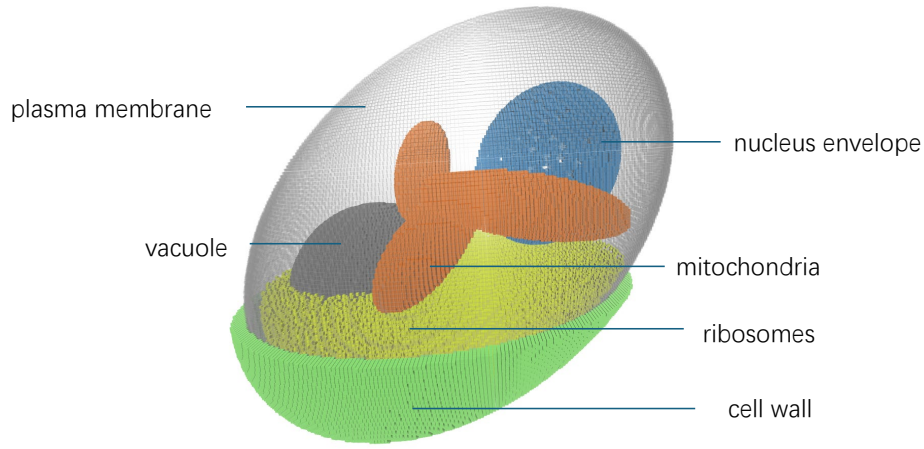

Fig 3. 3D spatial geometry of budding yeast. To enhance visibility, only a subset of ribosomes is displayed. The vacuole is shown in gray, the nuclear envelope in blue with nuclear pores as empty holes. Mitochondria appear in orange, ribosomes in yellow, the plasma membrane in transparent gray, and the cell wall in green/lime.

0.1.3 Ribosome Distribution without ER

The ribosome dimensions in budding yeast are approximately $25.4\,\text{nm} \times 27.8\,\text{nm} \times 26.7\,\text{nm}$ [13]. Given that our lattice spacing is $28\,\text{nm} \times 28\,\text{nm} \times 28\,\text{nm}$, each ribosome was modeled as occupying one lattice cube. According to BioNumbers [11], the total number of ribosomes per budding yeast cell is roughly 1.8×10^5 [14]. Ribosomes were uniformly distributed throughout the cytoplasm by randomly selecting lattice sites not overlapping with existing intracellular structures. Although alternative reports indicate ribosome counts ranging from 105,000 to 380,414 [15–17], simulations showed that variations within this range had minimal impact on the final results, as the number of translating ribosomes during the first 60 minutes remained below 150, see Figure S1.

0.1.4 Endoplasmic reticulum modeling

We developed a novel method to construct the ER geometry based on available electron and fluorescence miscroscopy data [18]. Studies on budding yeast have shown that the ER differs significantly from the tubular network structures typically observed in

mammalian and plant cells [19, 20]. The yeast ER consists primarily of large curved sheets near the plasma membrane (peripheral ER, pmaER) and around the nuclear envelope (cisternal ER, cecER), connected by sparse tubular structures (tubular ER, tubER) [18, 21].

The volumetric occupancy of the entire ER was estimated at 2.2% [10]. The ER was decomposed into three regions: pmaER: 0.5 of total ER volume; tubER: 0.3 of total ER volume; cecER: 0.2 of total ER volume. Based on Figure 1F in West *et al.* [22], the average thickness of pmaER and cecER sheets were 35.6 nm and 36.0 nm, respectively, with a 33.0 nm gap between the ER sheets and the adjacent membranes.

To construct the pmaER, we generated an ellipsoidal shell with the thickness of one lattice cube, reducing each radius by two lattice cubes compared to the plasma membrane:

$$\begin{aligned}\text{pmaShell} = \text{Ellipsoid}\Big[&\big(a_{\text{plasmamem}} - 1,\ b_{\text{plasmamem}} - 1,\ c_{\text{plasmamem}} - 1\big),\\ &\text{(plasma membrane angles)},\\ &\text{(plasma membrane center)}\Big]\\ -\ \text{Ellipsoid}\Big[&\big(a_{\text{plasmamem}} - 2,\ b_{\text{plasmamem}} - 2,\ c_{\text{plasmamem}} - 2\big),\\ &\text{(plasma membrane angles)},\\ &\text{(plasma membrane center)}\Big].\end{aligned} \tag{1}$$

The pmaER was then constructed by randomly assigning a number n of fragments with individual volumes $\{V_i : i \in [1, n]\}$ in the pmaShell such that $\sum_{i=1}^{n} V_i = V_{\text{pmaER}}$. The BFS (breadth-first search) algorithm was applied to iteratively grow regions within the pmaShell until the desired volume V_i was reached. This process was repeated n times, ensuring no overlap between fragments:

$$\begin{aligned}\text{pmaFragments}_i \cap \text{pmaFragments}_j = \emptyset \quad (i \neq j),\\ \text{pmaER} = \sum_{i=1}^{n} \text{pmaFragments}_i.\end{aligned} \tag{2}$$

The same procedure was applied to construct the cecER, using adjusted parameters. The tubER was modeled as tubular structures with cross-sectional diameters d randomly selected from the range 60–100 nm [23]. The total tubER length was calculated as $L = \frac{V_{\text{tub}}}{d^2}$. Tubules were generated by connecting randomly selected pairs of pmaER and cecER fragments until the available length was exhausted. The final structure is shown in Figure 9(a).

0.1.5 Ribosomes translating into the ER

To approximate the number of ribosomes that translate into the ER, we acquired in cell cryo-ET data of *S. cerevisiae* [24] and analyzed the proximity of the peptide exit tunnel sites of all ribosomes to the ER membranes (Figure 4). The dense globular ribosomes are clearly discernible in the tomograms (Figure 4A), enabling their localization with DeePiCt [25], which employs a 3D Convolutional Neuronal Network (CNN). The CNN prediction output was manually curated to achieve roughly a 95 % completeness of ribosome annotations in the data (Figure 4B). Based on all detected ribosomes, we generated a subtomogram average of 10,723 ribosomes with a resolution of 11.1 Å [24]. We determined the position of the peptide exit tunnel based on this average (Figure 4

(C)). Next, MemBrain seg [26] was used to automatically annotate all membranes in the tomograms. The 'find connected regions' ImageJ plugin (`https://github.com/fiji/VIB/blob/master/src/main/java/util/Find_Connected_Regions.java`) was used to assign labels to the different organelle membranes and export the binary mask of only the ER membranes which were present in 6 out of the 9 reconstructed tomograms. Napari [27] (`https://zenodo.org/records/15029515`) was used to manually clean up any errors in the ER segmentations. Finally, the distances of all peptide exit tunnels to the closest ER membrane were calculated using a custom python script. Based on the histogram of these distances, a cut-off distance of 8 nm was determined to identify translating ribosomes on the surface of the ER (Figure 9E-F). The surface area of the ER was calculated using the RegionFeaturesJ plugin (`https://github.com/ijtools/RegionFeaturesJ/releases/tag/v0.3.1`) in ImageJ to report the number of translating ribosomes per ER surface area. The regions analyzed in our cryo-ET data predominantly represent cortical ER (referred to as pmaER in [22]) and ER continuous with the nuclear envelope (cecER). Potential tubular ER (tubER) is not continuous with the nuclear envelope and can be hard to discern from Golgi. It was excluded from our calculations for stringency reasons.

A previous study using plastic-sections electron microscopy reports higher numbers for ribosomes located on the ER membrane surface [22] compared to the cryo-ET derived values determined in the present study (ER-associated ribosome density in Table 1). This discrepancy likely arises from different criteria for defining an ER-ribosome association. In the present study, a ribosome translating into the ER is defined by a distance of the peptide exit tunnel of below 8 nm, taking the orientation of the individual ribosomes into account. In contrast, the previous study includes all ribosomes within 5 nm of the ER membrane regardless of their orientation, thus potentially including ribosomes that were not actively translating into the ER.

For the first round of simulation (ER sim high-ribo), we used the previously reported average ribosome density value [22]. We then re-ran the simulation with the number of translating ribosomes on the ER surface determined based on our cryo-ET data (ER sim low-ribo). Here, we treated the determined value as pmaER density and adapted it for cecER and tubER proportionally. In both simulations, ribosomes were randomly assigned to lattice sites according to the calculated surface areas of the respective ER regions taking into account that the ER membrane proximal to the cell membrane is not decorated with ribosomes. The final number of ER-bound ribosomes was 15,452 and 7,715, which are within range of the median abundance of sec61 (YLR378C), reported as 17,267 according to data from SGD [28]. Sec61 is the only essential component of Sec61p ER translocation complex. The remaining free ribosomes were uniformly distributed throughout the cytoplasm in both simulations.

0.1.6 Final Geometry

The reconstructed geometry shown in Figure 9 (d), consisting of 10 spatial regions (extracellular region, cell wall, plasma membrane, cytoplasm, nuclear envelope, nucleoplasm, mitochondria, vacuole, ribosomes), was integrated into the Lattice Microbes v2.5 for spatially resolved stochastic simulations. For simulations including the ER, the reconstructed geometry included 16 spatial regions (extracellular region, cell wall, plasma membrane, cytoplasm, nuclear envelope, nucleoplasm, mitochondria, vacuole, ribosomes, cecER, cecER_ribosomes, tubER, tubER_ribosomes, pmaER, pmaER_ribosomes).

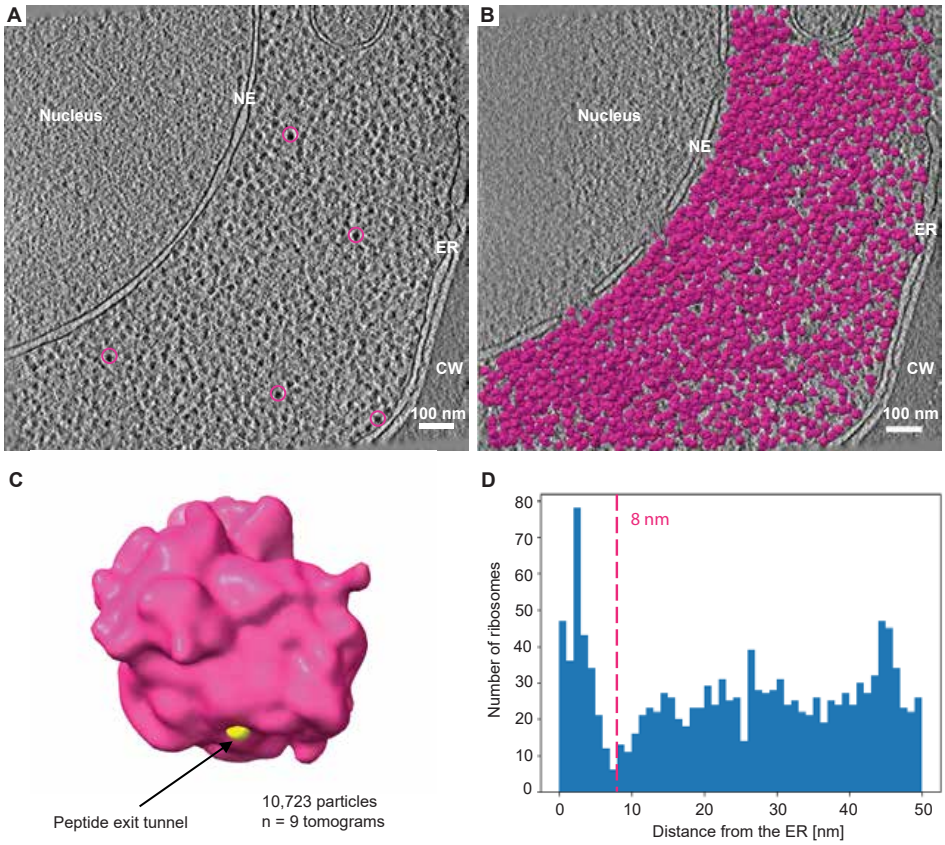

Fig 4. Number of translating ribosomes on ER membranes based on cryo-electron tomograms of *S. cerevisiae*. (A,B) Tomographic slice of an *S. cerevisiae* cell depicting the cytosol crowded with ribosomes (dense globular particles), the ER, the cell wall (CW) and the nucleus with the nuclear envelope (NE). (A) Individual ribosomes are encircled in magenta. (B) Example of comprehensive 3D annotation of all 80S ribosomes (magenta). (C) Ribosome subtomogram average from wildtype *S. cerevisiae* cells. Particle number, determined resolution and number of tomograms are indicated. The average was used to determine the coordinate of the peptide exit tunnel (centroid of the yellow sphere). (D) Histogram of the distances of all peptide exit tunnels to a binary segmentation of the closest ER membrane. A cut-off distance of 8 nm was determined to identify translating ribosomes on the surface of the ER.

0.2 Reaction-diffusion master equation(RDME)

The reaction-diffusion master equation (RDME) provides a powerful framework for spatially-resolved stochastic simulations of intracellular processes, combining particle-level stochastic reactions with spatial diffusion dynamics. In this study, we applied the RDME approach to simulate the galactose switch in *S. cerevisiae*, incorporating spatial heterogeneity derived from cryo-ET data. These simulations were performed using the Lattice Microbes (LM) software suite [3, 5, 29], which supports both well-stirred and spatially-resolved models. For RDME/spatially resolved models, LM explicitly incorporates spatial effects by discretizing the cellular volume into subvolumes v centered on a cubic lattice grid. Reactions occurring within each subvolume are assumed to be well-stirred and are simulated stochastically using the Gillespie algorithm [6], while particle diffusion between adjacent subvolumes is modeled using a diffusion operator.

$$\begin{aligned}\frac{dP(\mathbf{x},t)}{dt} &= \mathbf{R}P(\mathbf{x},t) + \mathbf{D}P(\mathbf{x},t) \\ &= \sum_{v}^{V}\sum_{r}^{R}\Big[-a_r(\mathbf{x}_v)P(\mathbf{x}_v,t) + a_r(\mathbf{x}_v-\mathbf{S}_r)P(\mathbf{x}_v-\mathbf{S}_r,t)\Big] \\ &\quad + \sum_{v}^{V}\sum_{\xi}^{i,j,k}\sum_{\alpha}^{N}\Big[-d^{\alpha}x_v^{\alpha}P(\mathbf{x},t) + d^{\alpha}\big(x_{v+\xi}^{\alpha}+1\big)P\big(\mathbf{x}+1_{v+\xi}^{\alpha}-1_v^{\alpha},t\big)\Big]. \qquad (3)\end{aligned}$$

The RDME governing these dynamics can be expressed as a sum of two terms: the chemical master equation (CME) in the subvolume that describes the reaction happens in it and a diffusion term accounting for inter-subvolume molecular movement. Specifically, the local CME governs stochastic chemical reactions within each subvolume v, while the diffusion operator describes the movement of particles of type along the x, y, and z directions, represented by indices i, j, k. The state of the system x, encapsulates the molecular counts of all species (genes, RNAs, and proteins) at any given time. Spatial heterogeneity arises naturally in these simulations, capturing differences in molecular distributions across subcellular regions, such as ribosome regions, nucleus, and cytoplasmic zones.

0.3 Multi-GPU Solver for RDME Simulation

To scale spatial stochastic simulations of the galactose switch in yeast, we implemented the MGPUMpdRdmeSolver, a multi-GPU extension of the existing MpdRdmeSolver in Lattice Microbes by Hallock *et al.* [5] to allow hybrid simulations. Our implementation partitions the three-dimensional simulation domain along the Z-axis, distributing workloads across multiple GPUs while minimizing inter-device communication overhead.

Each GPU independently processes its assigned subdomain, exchanging only the necessary boundary data during synchronization phases. To optimize runtime performance, we leverage asynchronous CUDA streams that overlap computation with communication in the overlapping regions. Peer-to-peer (P2P) memory transfers via NVLink or PCIe further accelerate data exchange between GPUs by avoiding costly host memory transfers. Moreover, custom packing and unpacking routines compress boundary updates into contiguous buffers, thereby reducing data movement. Figure 5 illustrates how multiple GPUs partition the simulation space and exchange boundary area data.

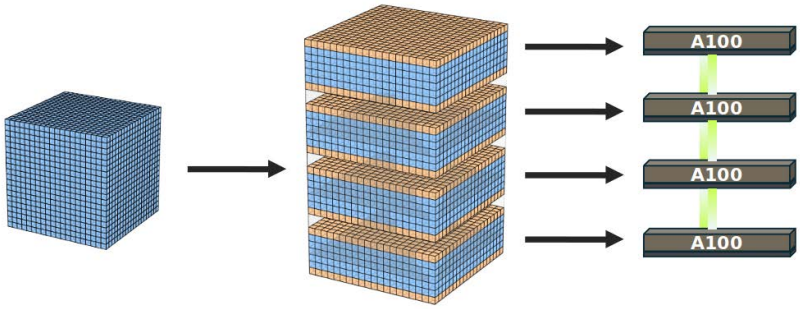

Fig 5. Coarse-grained lattice layout in Multi-GPU solvers: The continuous cellular space is first coarse-grained into a 3D lattice(in blue, left). This lattice is then evenly partitioned into four slices, each including two additional apron regions on the top and bottom of the cell region (shown in orange) to allow inter-slice communication. Each slice is assigned to a separate A100 GPU for parallel computation. After local computations are completed, neighboring slices exchange information about particles in the apron regions to ensure consistency across GPU boundaries.

Each GPU is bounded to a dedicated CPU thread, and these threads are synchronized by *pthread* barriers and *mutexes* that prevent race conditions. Within each thread, CUDA synchronization APIs are used to maximize parallelism.

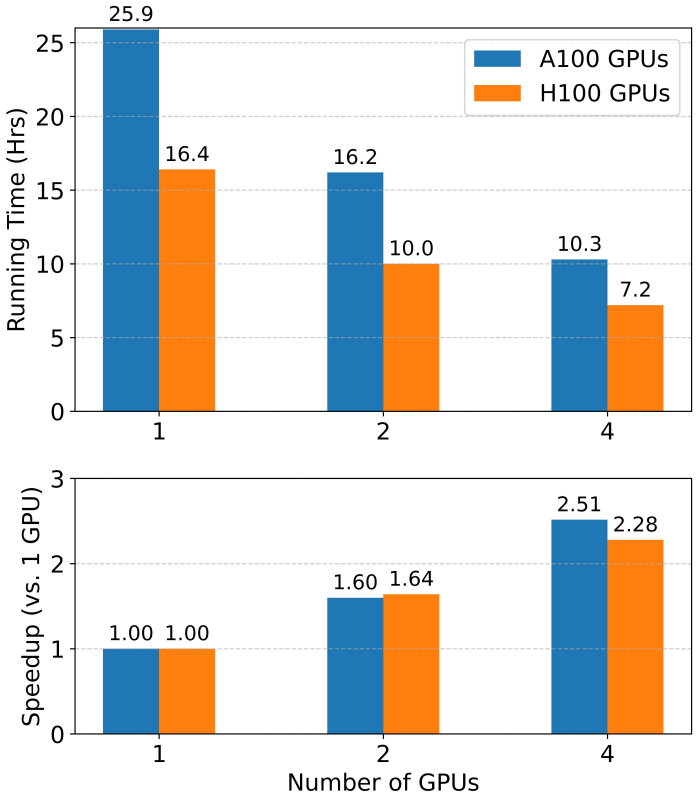

Fig 6. Computational Performance of Yeast RDME-ODE Simulations on A100 vs. H100 GPUs. Simulations represent 1 hour of biological time and were conducted using 1, 2, and 4 GPUs. The top panel shows the total wall-clock runtime in hours, with H100 GPUs consistently outperforming A100 GPUs across all configurations. The bottom panel illustrates the speedup relative to the 1-GPU runtime for each hardware type. Both GPU architectures exhibit sublinear scaling, with A100 achieving a maximum speedup of 2.51× and H100 reaching 2.28× with 4 GPUs.

We run the RDME simulations on Delta (AMD EPYC 7763 "Milan" CPU and Ampere 100 GPU) and Delta AI (NVIDIA Grace CPU and Hopper 100 GPU). Figure 6 shows the benchmark statistics of running single-GPU and multi-GPU solvers on our yeast model, and the 4-GPU solver demonstrates a 2.5-time speedup compared to the 1-GPU solver. Consequently, multi-GPU solvers can enable simulations of larger cellular volumes and longer timescales, fully capturing the spatial heterogeneity of the yeast galactose network while maintaining high computational efficiency.

0.4 Hybrid RDME-ODE method

We employed the hybrid RDME-ODE framework to efficiently simulate spatially resolved gene expression and metabolism in budding yeast, using stochastic methods for low-copy processes and ODEs for high-copy metabolic reactions. Notably, the bimolecular reaction $G3 + GAI \rightarrow G3i$, characterized by a low copy number of G3 and a high copy number of GAI, poses computational challenges when directly included in the RDME framework. Direct incorporation significantly slows down the RDME simulations and leads to spatially crowded subvoxels due to excessive galactose molecules. To address this, we converted the bimolecular reaction into a pseudo-first-order reaction $G3 \rightarrow G3i$ by redefining its kinetic parameter as

$k' = k \cdot [\text{GAI}]$, where k represents the original kinetic rate constant and [GAI] denotes the intracellular concentration of GAI. This modification maintains biological accuracy while significantly enhancing computational efficiency. This conversion and parameter update are handled dynamically by the *setReactionRate* function within the simulation hook, newly implemented here for compatibility with multi-GPU solvers.

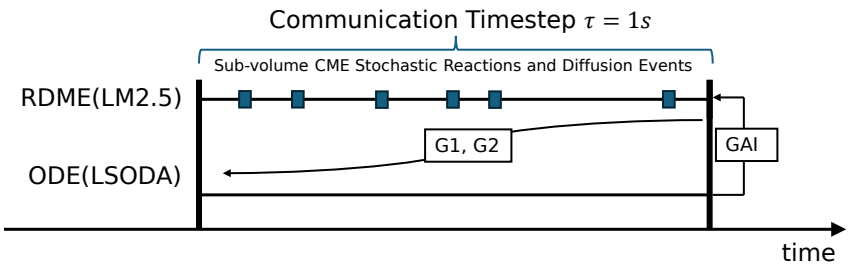

Fig 7. Hook schematics for the communication between RDME and ODE simulation.

Communication between the RDME and ODE solvers occurs at regular intervals $\tau = 1s$ as depicted in Figure 7, determined based on the separation of timescales between slow stochastic reactions and faster deterministic metabolic processes [3]. At each communication step, the state of the RDME system (e.g., local particle counts) is updated to reflect the results of the ODE solver, and then the ODE part is performed, and communicate the species counts back to RDME and updates the kinetic parameters in RDME simulation.

Algorithm 1 Hybrid RDME-ODE Simulation of the Galactose Switch Using Lattice Microbes

```
Initialize simulation environment
Load spatial model and define domains (extracellular, cell wall, nucleus, etc.)
Specify molecular species
Define biochemical reactions (transcription, translation, degradation, etc.)
Assign diffusion coefficients
procedure HybridSimulation
    Initialize ODE system for transport and metabolism
    Initialize RDME system for spatial stochastic reactions
    while t < t_max do
        Execute RDME step (reaction-diffusion process)
        if time interval== hook interval then
            Update ODE state using RDME molecular counts
            Integrate ODE system over the interval
            Update RDME reaction rates based on ODE outputs
        end if
        Store system statistics and trajectory data
    end while
end procedure
```

0.5 Yeast Galactose Switch System

In our spatial RDME simulations of the galactose switch in Figure 1, genetic information processes were resolved with subvolume precision. The regulation events are

built in the nucleoplasm region for regulatory genes DG1, DG2, DG3, DG80 and DGrep (fluorescence reporter gene), non-regulatory gene DG4. For regulatory genes, each has 3 states: free(DGX), activated(DGX:G4d) and repressed(DGX:G4d:G80d). When genes are in activated states, the transcription starts and ends with the release of the messenger RNAs (mRNAs) in the same sublattice volume. For non-regulatory gene DG4, the transcription happens stochastically with a given rate. The messengers then diffuse from nucleosplasm to cytoplasm through nuclear pores. In the cytoplasm, mRNAs further diffuse into and bind to ribosomes for translation. The regulators consist of 3 proteins: G3, G4 and G80. G3 can bind to the cytoplasmic galactose GAI to form a complex G3i, which can further bind to the G80d in the cytoplasm. G3iG80d complex will prevent G80d from transport through the nuclear pore into the nucleoplasm.

The counts of G2 in the plasma membrane and G1 in cytoplasm created by the stochastic reactions occurring within time steps of length τ are communicated to the ODE model, which then performs galactose transport and metabolism via galactokinase G1. This backward-updating hybrid scheme ensured efficient and accurate coupling between spatially-resolved stochastic reactions and deterministic metabolic processes.

For reactions modeled by the RDME, it is necessary to define the spatial regions within which each reaction is permitted to occur (see Tables in SI). Additionally, diffusion behaviors must be specified for each molecular species, including diffusion within a given region type and diffusion across boundaries between different regions, as detailed in (Table S12 in SI).

For the initial abundance of each species, we used the values reported in Ramsey *et al.* [1], rounding each to the nearest integer. For molecular species that are present in multiple cellular compartments, we distributed their initial counts proportionally according to regional volumes. The initial counts used in the RDME simulations are summarized in Table S2-3 in SI. Gene copy numbers were set to one and placed randomly in the nuclear envelope in their repressed state (GalX:G4d:G80d), consistent with biological expectations in the absence of induction. These repressed genes are assumed to be immobile (non-diffusive) throughout the simulation. In contrast, G4, which is not under regulatory control in the model, is constitutively transcribed. For the mutant conditions, we removed regulatory constraints on G3 and G80, allowing them to be transcribed continuously. All mRNAs were initialized with zero copy numbers, except for mRNA for G3 and Grep (R3, Rrep). The protein species G1, G3, and the reporters (GFP/YFP) were randomly distributed in the cytoplasm at initialization, while G2 was localized to the plasma membrane. G4d was initialized in the nucleoplasm. G80 and G80d were randomly distributed between cytoplasm and nucleoplasm in proportion to the volume ratio of the two regions. Ribosomes were also placed in their respective compartments to support mRNA translation. The internal galactose concentration was initialized to zero, reflecting experimental conditions in which cells were first cultured in a non-inducing medium (raffinose) before galactose exposure. External galactose was treated as a constant input set by the user throughout the simulation. The choice to start from a repressed gene state and zero internal galactose reflects the experimental protocol [1], where the induction dynamics were measured upon switching cells from raffinose to galactose.

Results and Discussion

0.6 Intracellular spatial heterogeneity enhances galactose transport in RDME-ODE compared to CME-ODE models

Using the galactose transporter G2 as a representative example (Figure 8), we observe that spatial heterogeneity indeed alters system dynamics. Initially, all genes begin in the inhibited state(DGX:G4d:G80d); however, in the spatially-resolved RDME-ODE model, genes exhibit significantly higher probability of transitioning to and kept in the activated state compared to the well-mixed CME-ODE model (Figure 8 (a)). Our analysis shows that spatial geometry plays a critical role in genetic information processing within the galactose utilization network.

The reason DG2 has a higher probability of remaining in activated states is primarily due to an initial asymmetry in diffusion probabilities. Specifically, the repressor G80d has a greater likelihood of diffusing out of the nucleoplasm rather than into it, resulting in an increased probability of gene activation. According to kinetic parameters, G80d demonstrates stronger regulatory effects compared to G4d, reflected in its lower dissociation probability despite having similar binding kinetics.

This asymmetry can be quantified using average search times. For G80d diffusion within the nucleoplasm (Figure 8 (e)), we consider the time required to locate a nuclear pore from the nucleus center. Given that the nuclear dimensions along the a, b, and c axes are roughly equal, we approximate the nucleus as a sphere with radius $R_{\text{nuc}} = 1\ \mu m$. For particles diffusing inside a spherical domain of radius R with absorbing patches (pores) of fractional area ϕ, the average escape time (τ) can be estimated using the well-established formula [30, 31]:

$$\tau = \frac{R^2}{3D\phi} \tag{4}$$

For our model, the fractional area occupied by nuclear pores is:

$$\phi = \frac{A_{\text{pores}}}{S_{\text{nuc}}} = \frac{N \cdot \pi \cdot r_{\text{pore}}^2}{4\pi R_{\text{nuc}}^2} = \frac{139 \times \pi \times 0.042^2 \mu m^2}{4\pi \times 1^2 \mu m^2} \approx 0.06 \tag{5}$$

Thus, the average time for G80d to diffuse out of the nucleus is:

$$\tau_{\text{out}} = \frac{(1\mu m)^2}{3 \times 1\mu m^2/s \times 0.06} \approx 5.44s \tag{6}$$

When treated as a first-order reaction, as we have in the CME-ODE model, this yields a rate constant:$k_{\text{out}} \approx \tau_{\text{out}}^{-1} \approx 11.03/min$

Conversely, for G80d diffusing into the nucleus through nuclear pore complexes, the particle must first locate a pore and subsequently enter it. By approximating nuclear pores as absorbing spheres and applying the Smoluchowski 3D first-passage diffusion approximation, the average inward diffusion time (τ_{in}) is:

$$\tau_{\text{in}} \approx \frac{V_{\text{cyto}}}{4\pi D R_{\text{nuc}} \phi} \tag{7}$$

Assuming a spherical yeast cell with radius $R_{plasma\,mem} = 2\,\mu$m, the estimated average time for G80d to diffuse into the nucleus is approximately 38.1s, corresponding to the following: $k_{\text{in}} = \tau_{\text{in}}^{-1} \approx 1.57/min$

This substantial asymmetry in reaction kinetics contrasts sharply with the symmetric diffusion conditions in the CME-ODE model, where $k^{\text{CME-ODE}}\text{in} = k^{\text{CME-ODE}}\text{out} = 500/min$. This kinetic asymmetry explains the initial drastic reduction in G80d abundance observed in the RDME-ODE model relative to the CME-ODE model.

Genes maintain higher probabilities of remaining in activated states primarily due to reduced propensities, making state transitions less likely. Specifically, the effective propensities for first-order and second-order reactions are diminished in spatially heterogeneous environments due to reactant compartmentalization and the reduced volume from the entire cell to individual subvoxels.

Explicitly, for first-order reactions, the propensities are:

$$a_{\text{CME}} = k \cdot N_{a,\text{total}} \tag{8}$$

$$a_{\text{RDME}} = k \cdot N^{i}_{a,\text{subvoxel}} \tag{9}$$

where k is the reaction rate constant, Na, total is the total reactant count in the whole cell, and $N^{i}_{a,\text{subvoxel}}$ is the reactant count in subvoxel i. Thus, the relationship is:

$$a\text{RDME} = a_{\text{CME}} \cdot \frac{1}{N_{\text{subvoxels}}} < a_{\text{CME}}, \quad N_{\text{subvoxels}} > 1 \tag{10}$$

For second-order reactions, propensities are similarly adjusted:

$$a_{\text{CME}} = k \cdot \frac{N_{a,\text{total}} \cdot N_{b,\text{total}}}{V_{\text{total}}} \tag{11}$$

$$a_{\text{RDME}} = k \cdot \frac{N_{a,\text{subvoxel}i} \cdot Nb, \text{subvoxel}j}{V\text{subvoxel}_i} \tag{12}$$

Here, $N_{b,\text{total}}$ and $N_{b,\text{subvoxel}j}$ represent the total and subvoxel-specific counts of the second reactant, respectively; $V\text{total}$ and $V_{\text{subvoxel}i}$ denote the total cell and subvoxel volumes. Assuming well-mixed conditions, $Ni, \text{total} = N_{i,\text{subvoxel}i} \cdot N\text{subvoxels}$ and $V_{\text{total}} = V_{\text{subvoxel}i} \cdot N\text{subvoxels}$, yielding:

$$a_{\text{RDME}} = a_{\text{CME}} \cdot \frac{1}{N_{\text{subvoxels}}} < a_{\text{CME}} \tag{13}$$

The increased probability of gene activation leads to enhanced mRNA production in the RDME-ODE model. Subsequently, the high local concentration of ribosomes in the cytoplasmic compartments facilitates efficient translation, resulting in accelerated G2 protein synthesis compared to the CME-ODE model (Figure 8 (c)). In the spatial model, G2 proteins experience the directional diffusion toward the cell membrane in $\tau = \frac{\langle l^2 \rangle}{6D} \approx 1.5\,\text{s}$, establishing concentration gradients that further enhance transport efficiency. These spatial effects eventually lead to elevated intracellular galactose concentrations in FIgure 8 (d), highlighting how spatial organization can influence the dynamics of the galactose switch system. Additionally, we used the RDME-ODE model to reproduce the rapid increase in reporter levels (GFP/YFP) observed in the mutant strain compared to the wild type shown in Figure S3, consistent with the original experimental findings [1].

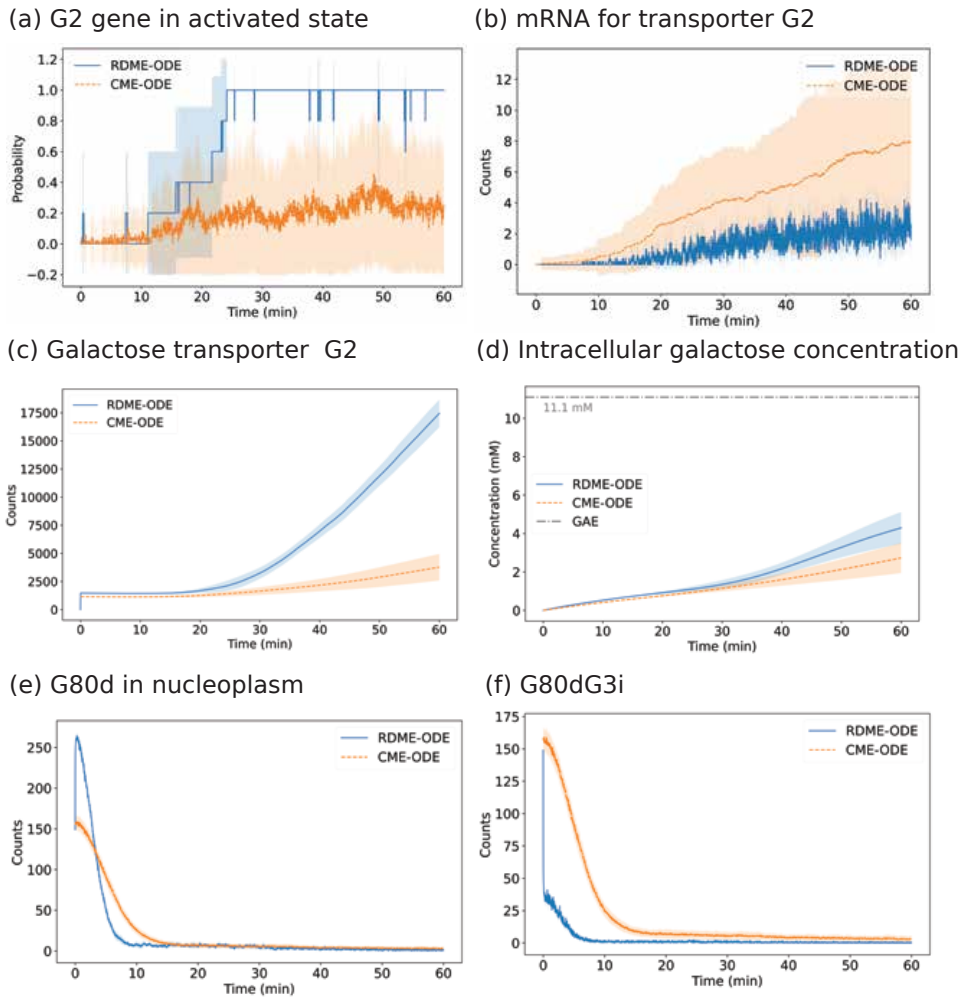

Fig 8. Comparison of G2-related species and intracellular galactose (GAI) concentration between our RDME-ODE model and the CME-ODE model [3]. (a) Probability of the transporter gene in the activated state (DG2:G4d). (b) Abundance of total mRNA (R2). (c) Abundance of galactose transporter G2. (d) Total intracellular galactose concentration(sum of GAI, G1GAI, G2GAI, and G3i).(e) Abundance of G80d in nucleoplasm. (f) Abundance of G80d in cytoplasm. Both simulations were performed for 60 minutes with 11.1 mM constant external galactose concentration. For the RDME-ODE simulations, we ran five replicates using the geometry without the ER. Identical kinetic parameters were applied to both models, except that the first-order diffusion reaction governing G80 transport between the cytoplasm and nucleus in the CME-ODE model was replaced with explicit diffusion events.

0.7 The endoplasmic reticulum creates temporal delays in membrane protein transport

We first reconstructed the ER as three distinct regions: the nuclear envelope-associated ER (nucER), the plasma membrane-associated ER (pmaER), and the tubular ER (tubER). Next, we added ER-attached ribosomes based on density data obtained either from West *et al.* [22] or from our own measurements.

To determine the influence of the ER on membrane protein transport, we compared

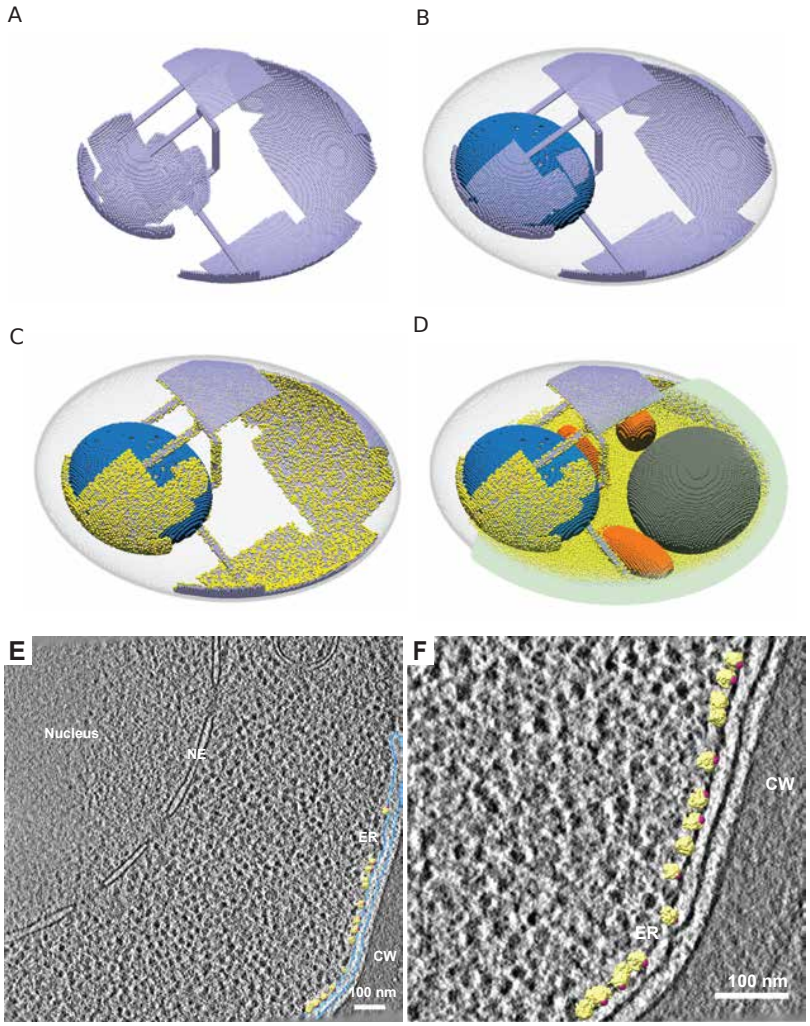

Fig 9. 3D modeling of the ER and ER-attached ribosome density experimental results. (a) Reconstructed ER with pmaER, tubER, and cecER. (b) ER wtih nucleus envelope and plasma membrane. (c) ER-attached ribosomes; the pmaER, which faces the plasma membrane, has very few ribosomes, so none are attached in the geometric model. (d) Final spatial geometry model for simulation with ER; for clarity, only a portion of the cyto-ribosomes are shown.(E) Ribosomes with an exit tunnel (magenta sphere) less than 8 nm from the closest ER membrane back-projected into the tomogram in accordance with their original position. The binary ER membrane segmentation is overlaid in blue. (F) Zoom in of (E) showing the orientation of the peptide exit tunnels with respect to the ER membrane.

RDME-ODE simulations under two distinct scenarios: with and without ER. In the ER-inclusive model, we further explored two distinct sub-scenarios that differ in the number and distribution of ER-associated ribosomes available for membrane translation. In all three cases, kinetic and diffusion parameters were kept constant, with biologically realistic spatial constraints applied only in the ER-inclusive conditions.

ER Region	Literature Range	ER high-ribo value	ER low-ribo value
cecER	600–1100	850	424
pmaER	550–900	725	362
tubER	250–400	325	162

Table 1. Comparison of ribosome surface densities on ER regions.

In ER-highRibo, we used average ribosome densities consistent with quantitative measurements from West's measurements [22], while in ER-lowRibo, we assigned a reduced number of ER-attached ribosomes based on our cryo-ET data. In both ER-inclusive cases, translation of the galactose transporter G2 was restricted to ER-bound ribosomes, leading to co-translational insertion into the ER and subsequent trafficking through the secretory pathway to the plasma membrane. While the total number of G2 transporters reaching the membrane over the first 20 minutes remained comparable across all conditions, a notable reduction in membrane-localized transporters was observed in the ER-inclusive simulations (Figure 10(d)). This reduction occurs for two reasons. First, since there are far fewer ER-attached ribosomes available for translation, free mRNA has a harder time finding a ribosome to initiate translation, compared to the no-ER case shown in Figure 10(a) and (b). Second, ER-mediated diffusion through complex, irregular, and tubular geometries inherently requires more time than direct cytoplasmic diffusion. As a result, many transporters remain in the cytoplasmic region (which includes the ER), in contrast to the no-ER cases shown in Figure 10(c). At the current diffusion rate, a transporter takes roughly 1 second to reach the plasma membrane. Additionally, transporters tended to accumulate in plasma membrane regions proximal to tubular ER structures. Consequently, intracellular galactose concentrations show significant differences across the simulations in Figure 10(e). In the no-ER case, concentrations reached approximately 4.5 mM, whereas in the ER-inclusive simulations, ER-highRibo averaged 2 mM and ER-lowRibo averaged 1 mM. These results suggest that intracellular galactose import is highly sensitive to transporter abundance at the plasma membrane.

Additionally, to evaluate the effect of the density of reduced ER-associated ribosome, we compared outcomes from two distinct simulations. The relative activation of the G2 gene and abundance of G2 mRNA remained consistent across both simulations. However, a discrepancy emerged in G2 protein levels, with an approximate difference of 2,000 molecules. This discrepancy can be attributed to decreased translation efficiency, as G2 mRNA is exclusively translated by ER-bound ribosomes. These findings underscore how ER spatial organization profoundly shapes the kinetic dynamics of gene expression and protein trafficking within the galactose regulatory network.

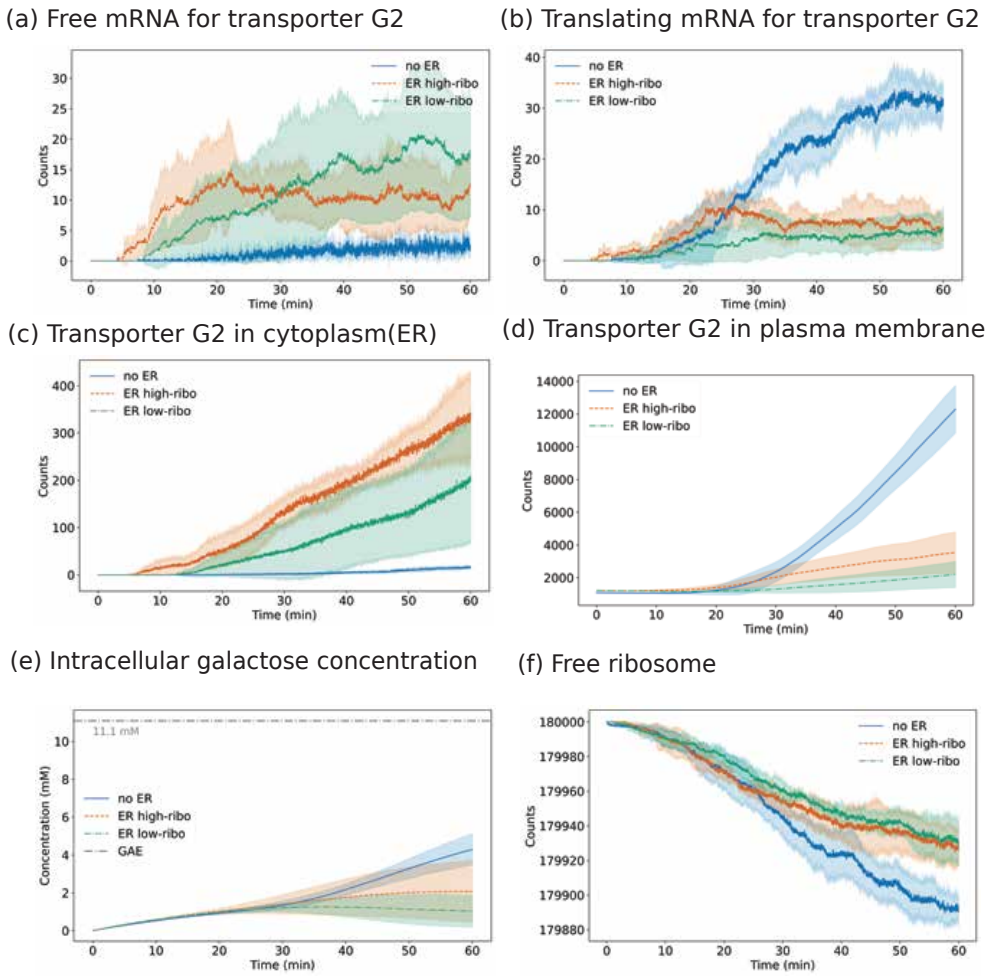

Fig 10. Comparison of intracellular galactose (GAI) and transporter(G2) related species between the model without ER and ER with different ER-associated ribosome density for ER high-ribo and ER low-ribo. (a) the abundance of free mRNA for transporter(R2). (b) the abundance of translating mRNA for transporter(R2). (c) the abundance of transporter in cytoplasm (including ER if present). (d)the abundance of galactose transporter G2 in plasma membrane. (e) Intracellular galactose concentration. (f) the abundance of free ribosomes not binding to any mRNA. All simulations are performed 60 minutes with $11.1mM$ external galactose concentration. 5 replicates per case.

0.8 Limited ribosome availability significantly constrains protein production

The galactose switch system operates under translational constraints because its mRNAs must compete with those of other cellular genes for access to the shared pool of free ribosomes. Technically, not all free ribosomes can be used to translate mRNA for the galactose switch system, as other cellular processes occupy the translational machinery. Here we assume that the ribosomes that translate the mRNA for the galactose switch system should roughly be proportional to the mRNA abundance for the galactose switch system compared to all the mRNA in the yeast. We estimated the

effective ribosome number using mRNA abundance to determine the number of available ribosomes for the galactose switch system. [7, 8] Since the reporter has the same promoter as GAL1, we used the mRNA abundance of GAL1 for Grep. We therefore assume that 2102 ribosomes (0.0117% of total ribosomes) are utilized while the rest are set into a silent state that only serve as an obstacle for diffusion in the cytoplasm. As expected, even though the system tries to produce more mRNA for G2, the G2 level is much lower than those having all 180,000 ribosomes available as shown in Figure 11. Unsuprisingly, the G2 level is much lower and so is intracellular galactose GAI. The G80dG3i is lower in the effective ribosomes case, but the relative level is not that much lower compared with ER and no ER case. This suggests that higher cytoplasmic concentrations of G3 lead to increased binding of G80d, which limits G80d's entry into the nucleus and thus shifts the system toward gene activation. Therefore, there are more mRNA produced for all the genes, but the G2 level is much lower.

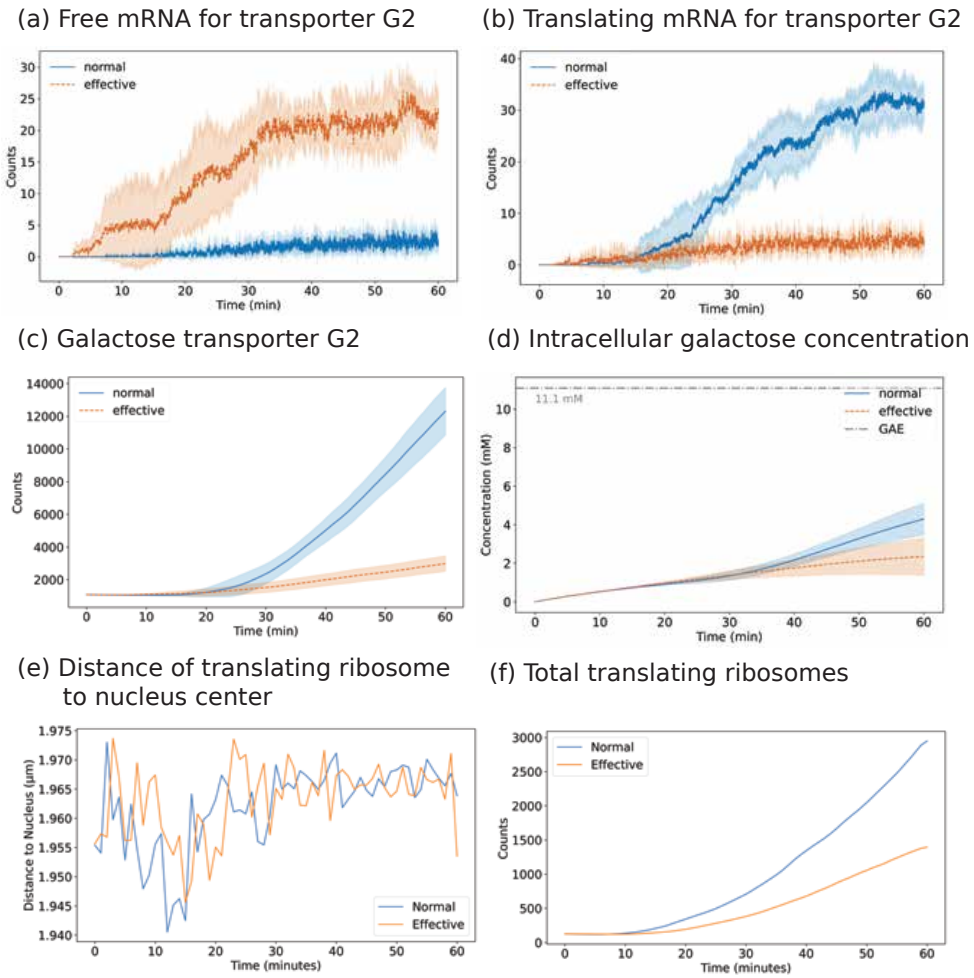

Fig 11. Comparison between effective ribosomes and all ribosomes in RDME-ODE. (a) the abundance of free mRNA for transporter G2. (b) the abundance of translating mRNA for transporter G2 (3) the abundance of galactose transporter G2. (d) the concentration of intracellular galactose GAI. (e) the average distance of translating ribosomes to the center of nucleus .(f)the average accumulated counts of translating ribosomes. Simulations are performed 60 minutes with $11.1mM$ external galactose concentration. The geometry without ER is used, same kinetic parameters and diffusion coefficients are used.

Conclusion

448

Our study presents a significant advancement in the computational modeling of intracellular processes by integrating spatial heterogeneity with stochastic and deterministic simulation approaches. Our hybrid RDME-ODE framework, incorporating cryo-ET data, provides some new insights into how spatial organization, ER and ribosome availability influences the behavior of the galactose switch in *Saccharomyces cerevisiae*.

The integration of spatial heterogeneity revealed several critical insights that would be overlooked in well-mixed models. First, our spatially resolved simulations demonstrated that the physical separation of molecular species across subcellular compartments significantly alters reaction dynamics compared to well-mixed CME-ODE models. The spatial segregation of regulatory molecules, particularly the sequestration of G80d in the cytoplasm by G3i, enhances the activation probability of genes in the nucleus, leading to increased mRNA production and ultimately higher transporter protein levels. Second, our incorporation of the ER revealed a temporal delay in membrane protein transport that is absent in models lacking spatial resolution. The requirement for G2 mRNA to locate ER-bound ribosomes, followed by the translated protein's extended diffusion path through the ER network to reach the plasma membrane, leading to the reduced transporter abundance on plasma membrane. Despite lower G2 transporter levels in the ER-inclusive model, intracellular galactose concentrations remained comparable between models with and without ER, suggesting there might be an optimal abundance of transporter to import external galactose. Third, our analysis of ribosome availability demonstrated that protein production is significantly constrained by the limited pool of ribosomes available for translating specific mRNAs. By incorporating a more realistic estimate of effective ribosome numbers based on mRNA abundance data, we observed substantially reduced protein production despite elevated mRNA levels.

While our model represents a significant advance in spatially resolved biochemical simulations, several limitations and opportunities for future work remain. The computational intensity of RDME-ODE simulations restricted our ability to perform extensive replicates, particularly for long-duration simulations. Additionally, our static spatial model does not account for dynamic changes in cellular architecture over time, such as membrane remodeling or organelle biogenesis, which may influence system behavior during extended simulations.

While our model marks a significant advance in spatially resolved biochemical simulations by integrating reaction-diffusion and deterministic dynamics in a realistic cellular architecture, several limitations remain that present opportunities for future refinement. This constraint may affect the statistical robustness of long-timescale phenomena or rare-event dynamics. Additionally, the spatial architecture used here is only from a single static tomographic snapshot, which does not capture the dynamic structural remodeling that occurs during membrane trafficking, organelle biogenesis, or nuclear reorganization—processes likely to influence molecular diffusion and reaction rates. Moreover, while our model captures essential aspects of gene expression and molecular interactions, it currently omits several biologically important layers of regulation. These include post-translational modifications, protein turnover, and compartment-specific metabolic fluxes, which are critical for understanding the full spectrum of cellular function. The absence of integrated pathways for energy metabolism, lipid biosynthesis, and cell cycle control also narrows the model's applicability to broader physiological contexts.

In conclusion, our hybrid RDME-ODE approach represents a significant step toward bridging the gap between molecular-level stochastic events and cellular-level deterministic processes in spatially heterogeneous environments. By demonstrating the critical influence of spatial organization on genetic regulatory networks, our work

underscores the importance of incorporating spatial heterogeneity in computational models of cellular processes. The methodologies developed here provide a foundation for future whole-cell modeling efforts that integrate structural, molecular, and systems-level data to achieve a comprehensive understanding of cellular function for budding yeast.

Supporting information

S1 File. Simulation paramters and supplementary simulation. This file contains information on species names, reactions, and simulation parameters such as kinetic rates and diffusion coefficients. It also includes additional simulation results referenced in the main text.

S2 Video Videos for the RDME-ODE simulation trajectory in 60 minutes for normal geometry.

S3 Video Videos for the RDME-ODE simulation trajectory in 60 minutes for ER-included geometry.

S4 Video Videos for the RDME-ODE simulation trajectory in 60 minutes for normal geometry with effective ribosomes.

S5 Repository. Source code Github repository with instructions to run the code: https://github.com/Luthey-Schulten-Lab/Yeast_Galactose_Switch_RDMEODE.git

Acknowledgments

The authors thank David Bianchi and Troy Brier for the support and tutorship for using Lattice Microbes. We would also like to thank Sara Kathrin Goetz for acquiring the cryo-electron tomograms, the EMBL cryo-EM platform for instrument access, and Thomas Hoffmann and EMBL IT for computational support. J.M. was supported by a European Research Council starting grant (3DCellPhase 760067) and the EMBL. This project was supported by National Science Foundation Science and Technology Cneter for Quantitative Cell Biology DBI-2243257. T.W, MC.S. and ZLS are also partially supported by NSF DBI-2243257. Z.R.T. Research reported in this publication was supported by the Cancer Center at Illinois–Beckman Institute Postdoctoral Fellows Program sponsored by the Cancer Center at Illinois and the Beckman Institute for Advanced Science and Technology, University of Illinois Urbana–Champaign. The content is solely the responsibility of the authors and does not necessarily represent the official views of the program sponsors.

References

1. Ramsey SA, Smith JJ, Orrell D, Marelli M, Petersen TW, De Atauri P, et al. Dual feedback loops in the GAL regulon suppress cellular heterogeneity in yeast. Nature Genetics. 2006;38(9):1082–1087. doi:10.1038/ng1869.

2. Acar M, Becskei A, Van Oudenaarden A. Enhancement of cellular memory by reducing stochastic transitions. Nature. 2005;435(7039):228–232. doi:10.1038/nature03524.

3. Bianchi DM, Peterson JR, Earnest TM, Hallock MJ, Luthey-Schulten Z. Hybrid CME–ODE method for efficient simulation of the galactose switch in yeast. IET Systems Biology. 2018;12(4):170–176. doi:10.1049/iet-syb.2017.0070.

4. Earnest TM, Watanabe R, Stone JE, Mahamid J, Baumeister W, Villa E, et al. Challenges of Integrating Stochastic Dynamics and Cryo-Electron Tomograms in Whole-Cell Simulations. The Journal of Physical Chemistry B. 2017;121(15):3871–3881. doi:10.1021/acs.jpcb.7b00672.

5. Hallock MJ, Stone JE, Roberts E, Fry C, Luthey-Schulten Z. Simulation of reaction diffusion processes over biologically relevant size and time scales using multi-GPU workstations. Parallel Computing. 2014;40(5):86–99. doi:https://doi.org/10.1016/j.parco.2014.03.009.

6. Gillespie DT. Exact stochastic simulation of coupled chemical reactions. The Journal of Physical Chemistry. 1977;81(25):2340–2361. doi:10.1021/j100540a008.

7. Csárdi G, Franks A, Choi DS, Airoldi EM, Drummond DA. Accounting for Experimental Noise Reveals That mRNA Levels, Amplified by Post-Transcriptional Processes, Largely Determine Steady-State Protein Levels in Yeast. PLOS Genetics. 2015;11(5):e1005206. doi:10.1371/journal.pgen.1005206.

8. Li JJ, Chew GL, Biggin MD. Quantitating translational control: mRNA abundance-dependent and independent contributions and the mRNA sequences that specify them. Nucleic Acids Research. 2017;45(20):11821–11836. doi:10.1093/nar/gkx898.

9. Kremer JR, Mastronarde DN, McIntosh JR. Computer Visualization of Three-Dimensional Image Data Using IMOD. Journal of Structural Biology. 1996;116(1):71–76. doi:10.1006/jsbi.1996.0013.

10. Wei D, Jacobs S, Modla S, Zhang S, Young CL, Cirino R, et al. High-Resolution Three-Dimensional Reconstruction of a Whole Yeast Cell Using Focused-Ion Beam Scanning Electron Microscopy. BioTechniques. 2012;53(1):41–48. doi:10.2144/000113850.

11. Milo R, Jorgensen P, Moran U, Weber G, Springer M. BioNumbers—the database of key numbers in molecular and cell biology. Nucleic Acids Research. 2010;38(suppl_1):D750–D753. doi:10.1093/nar/gkp889.

12. Visser W, Van Spronsen EA, Nanninga N, Pronk JT, Kuenen JG, Van Dijken JP. Effects of growth conditions on mitochondrial morphology inSaccharomyces cerevisiae. Antonie van Leeuwenhoek. 1995;67(3):243–253. doi:10.1007/BF00873688.

13. Verschoor A, Warner JR, Srivastava S, Grassucci RA, Frank J. Three-dimensional structure of the yeast ribosome. Nucleic Acids Research. 1998;26(2):655–661. doi:10.1093/nar/26.2.655.

14. von der Haar T. A quantitative estimation of the global translational activity in logarithmically growing yeast cells. BMC systems biology. 2008;2:87. doi:10.1186/1752-0509-2-87.

15. Yamaguchi M, Namiki Y, Okada H, Mori Y, Furukawa H, Wang J, et al. Structome of Saccharomyces cerevisiae determined by freeze-substitution and serial ultrathin-sectioning electron microscopy. Microscopy. 2011;60(5):321–335. doi:10.1093/jmicro/dfr052.

16. Biswas SK. Quantitative three-dimensional structural analysis of Exophiala dermatitidis yeast cells by freeze-substitution and serial ultrathin sectioning. Journal of Electron Microscopy. 2003;52(>2):133–143. doi:10.1093/jmicro/52.2.133.

17. Warner JR. The economics of ribosome biosynthesis in yeast. Trends in Biochemical Sciences. 1999;24(11):437–440. doi:10.1016/S0968-0004(99)01460-7.

18. Manford AG, Stefan CJ, Yuan HL, MacGurn JA, Emr SD. ER-to-Plasma Membrane Tethering Proteins Regulate Cell Signaling and ER Morphology. Developmental Cell. 2012;23(6):1129–1140. doi:10.1016/j.devcel.2012.11.004.

19. Obara CJ, Moore AS, Lippincott-Schwartz J. Structural Diversity within the Endoplasmic Reticulum—From the Microscale to the Nanoscale. Cold Spring Harbor Perspectives in Biology. 2023;15(6):a041259. doi:10.1101/cshperspect.a041259.

20. Holcman D, Parutto P, Chambers JE, Fantham M, Young LJ, Marciniak SJ, et al. Single particle trajectories reveal active endoplasmic reticulum luminal flow. Nature Cell Biology. 2018;20(10):1118–1125. doi:10.1038/s41556-018-0192-2.

21. Gallo A, Vannier C, Galli T. Endoplasmic Reticulum–Plasma Membrane Associations: Structures and Functions. Annual Review of Cell and Developmental Biology. 2016;32(Volume 32, 2016):279–301. doi:10.1146/annurev-cellbio-111315-125024.

22. West M, Zurek N, Hoenger A, Voeltz GK. A 3D analysis of yeast ER structure reveals how ER domains are organized by membrane curvature. Journal of Cell Biology. 2011;193(2):333–346. doi:10.1083/jcb.201011039.

23. Shibata Y, Voeltz GK, Rapoport TA. Rough Sheets and Smooth Tubules. Cell. 2006;126(3):435–439. doi:10.1016/j.cell.2006.07.019.

24. Xie Y, Shu T, Liu T, Spindler MC, Mahamid J, Hocky GM, et al. Polysome collapse and RNA condensation fluidize the cytoplasm. Molecular Cell. 2024;84(14):2698–2716.

25. de Teresa-Trueba I, Goetz SK, Mattausch A, Stojanovska F, Zimmerli CE, Toro-Nahuelpan M, et al. Convolutional networks for supervised mining of molecular patterns within cellular context. Nature Methods. 2023;20(2):284–294.

26. Lamm L, Zufferey S, Righetto RD, Wietrzynski W, Yamauchi KA, Burt A, et al. MemBrain v2: an end-to-end tool for the analysis of membranes in cryo-electron tomography. biorxiv. 2024; p. 2024–01.

27. Gaifas L, Timmins J, Gutsche I. blik: an extensible napari plugin for cryo-ET data visualisation, annotation and analysis. bioRxiv. 2023; p. 2023–12.

28. Cherry JM, Hong EL, Amundsen C, Balakrishnan R, Binkley G, Chan ET, et al. Saccharomyces Genome Database: the genomics resource of budding yeast. Nucleic Acids Research. 2012;40(D1):D700–D705. doi:10.1093/nar/gkr1029.

29. Roberts E, Stone JE, Luthey-Schulten Z. Lattice microbes: High-performance stochastic simulation method for the reaction-diffusion master equation. Journal of Computational Chemistry. 2013;34(3):245–255. doi:10.1002/jcc.23130.

30. Berg HC, Purcell EM. Physics of chemoreception. Biophysical Journal. 1977;20(2):193–219. doi:10.1016/S0006-3495(77)85544-6.

31. Schuss Z, Singer A, Holcman D. The narrow escape problem for diffusion in cellular microdomains. Proceedings of the National Academy of Sciences of the United States of America. 2007;104(41):16098–16103. doi:10.1073/pnas.0706599104.

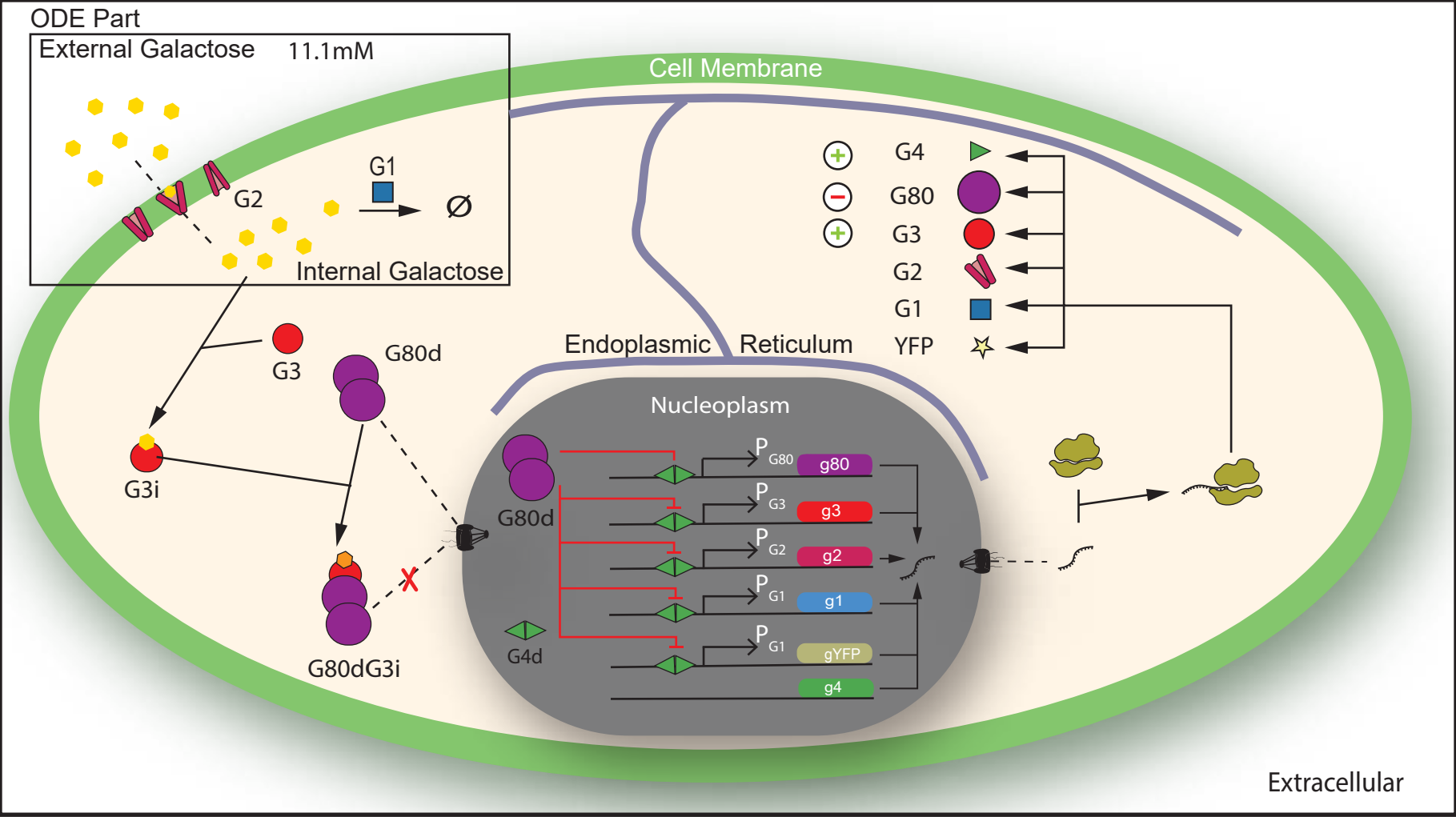
ODE Part
External Galactose
11.1mM
Cell Membrane
G1
G2
Ø
Internal Galactose
G4
G80
G3
G2
G1
YFP
G3
G80d
Endoplasmic
Reticulum
Nucleoplasm
G3i
G80d
G80dG3i
G4d
P G80
g80
P G3
g3
P G2
g2
P G1
g1
P G1
gYFP
g4
Extracellular

(a)

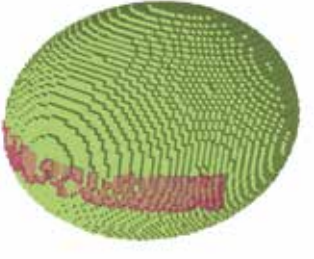

(b)

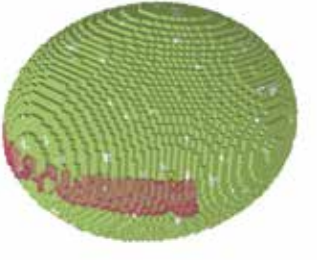

(c)

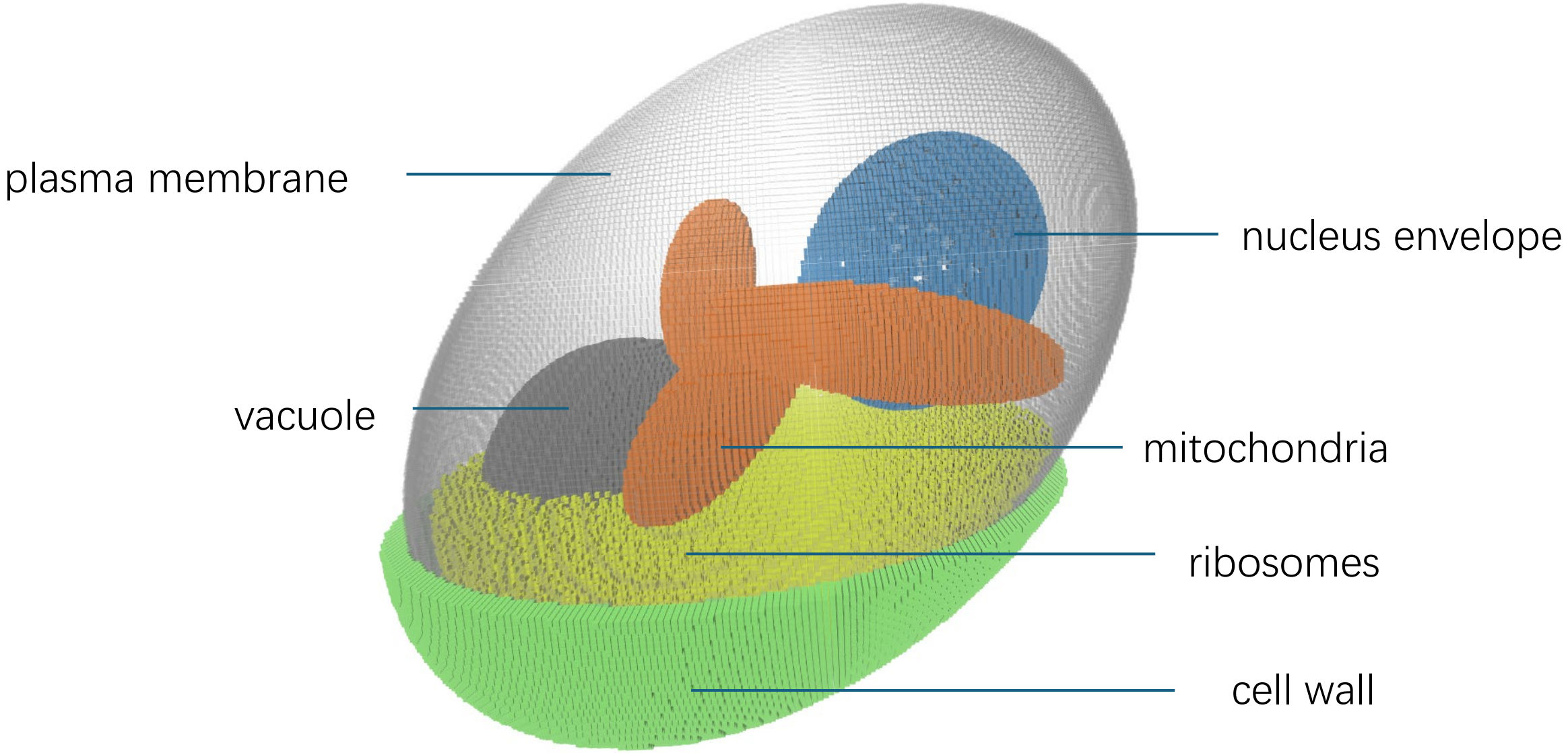
plasma membrane
nucleus envelope
vacuole
mitochondria
ribosomes
cell wall

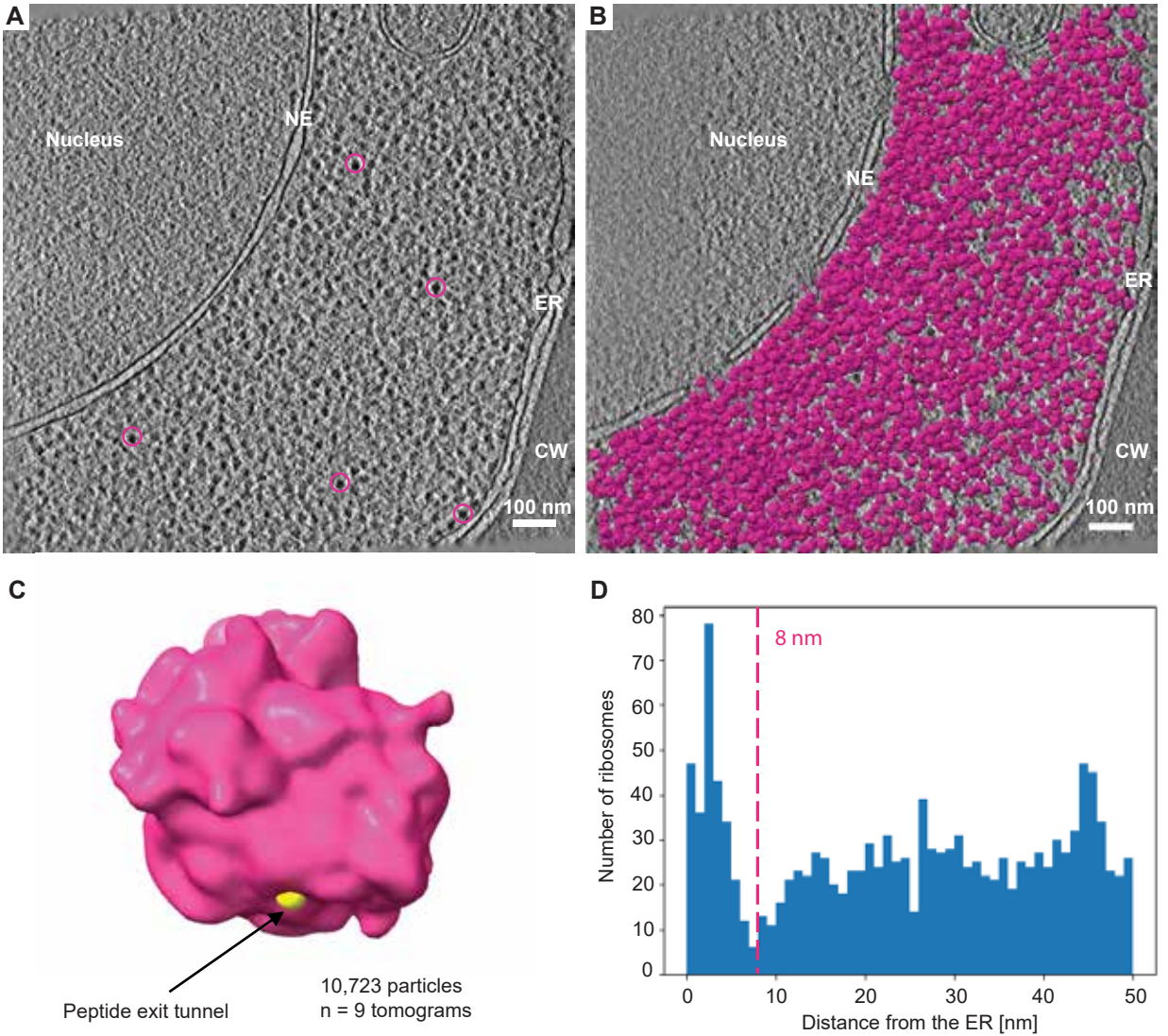
A
Nucleus
NE
ER
CW
100 nm
B
Nucleus
NE
ER
CW
100 nm
C
Peptide exit tunnel
10,723 particles
n = 9 tomograms
D
8 nm
Number of ribosomes
Distance from the ER [nm]
0
10
20
30
40
50
60
70
80

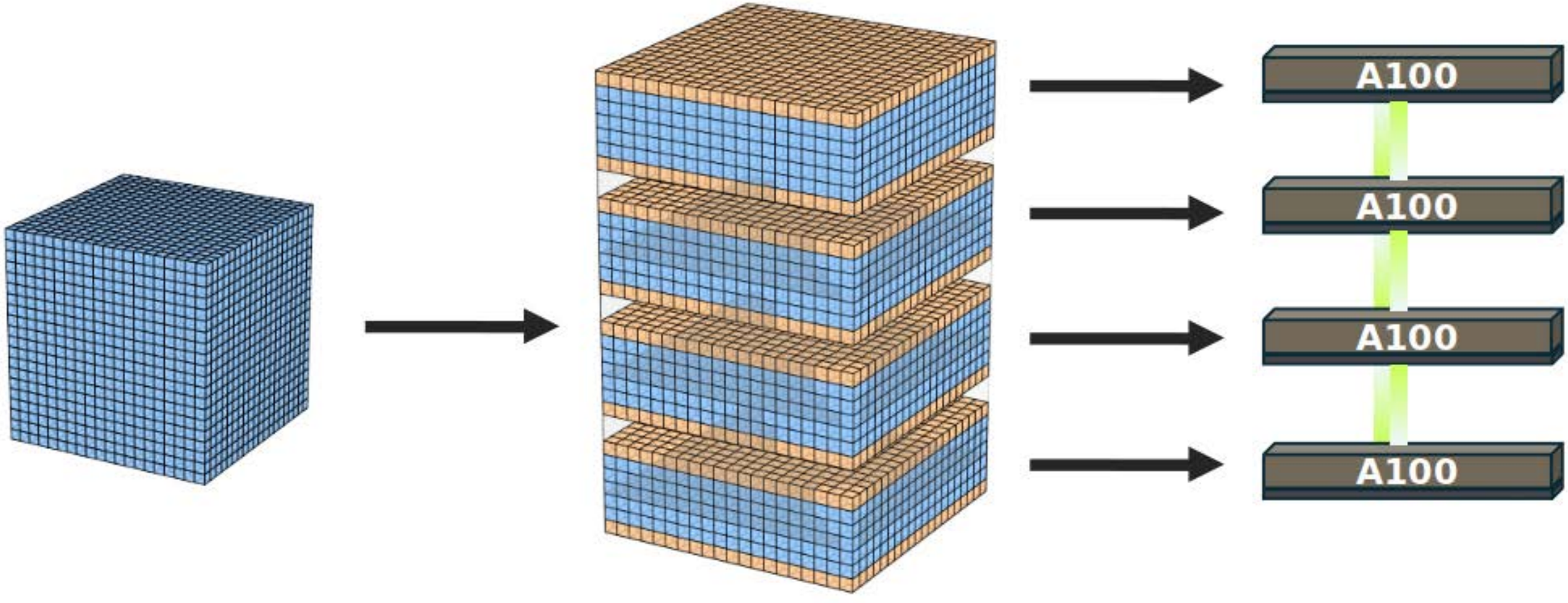
A100
A100
A100
A100

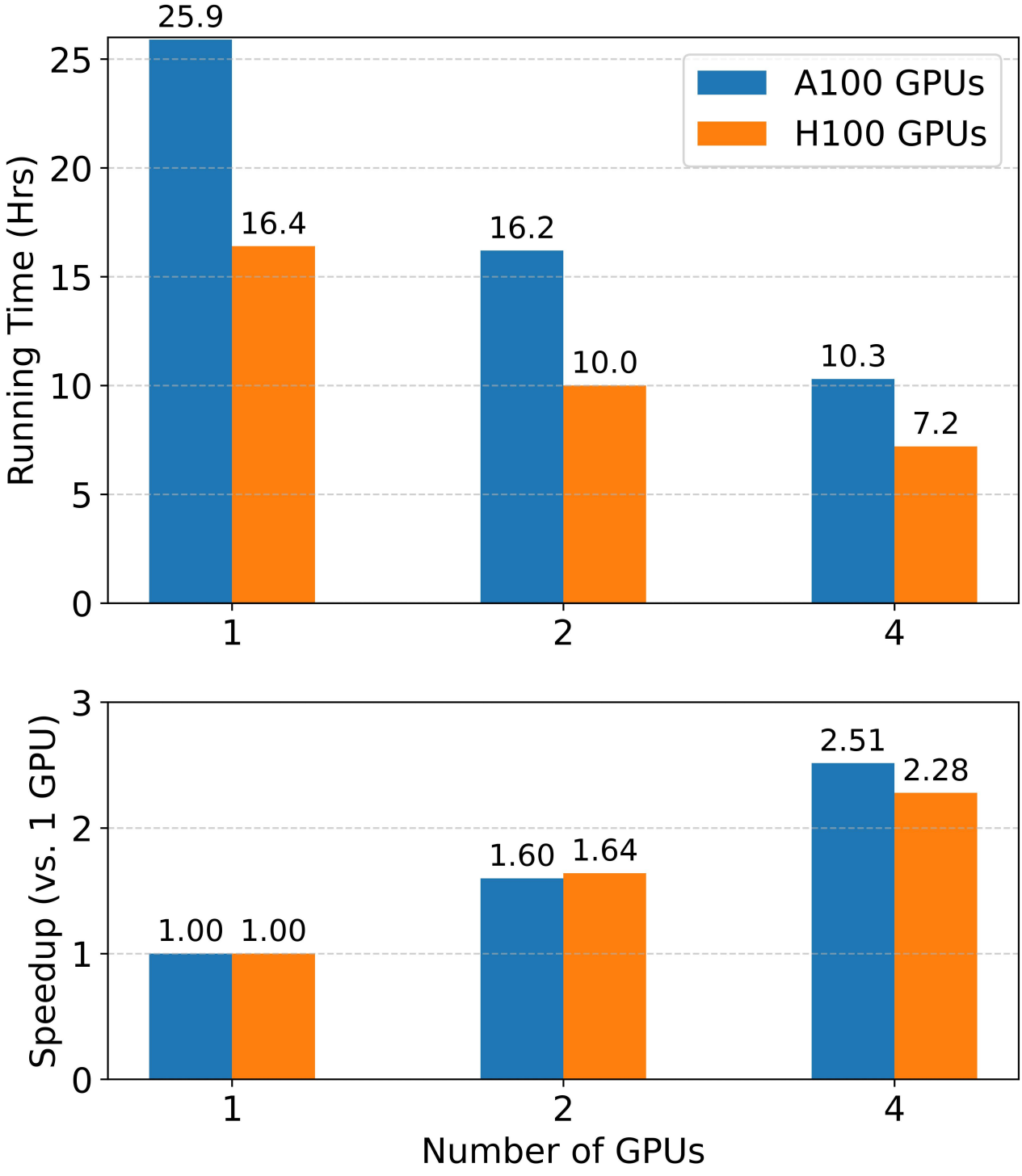
25.9
16.4
16.2
10.0
10.3
7.2
A100 GPUs
H100 GPUs
Running Time (Hrs)
0
5
10
15
20
25
1
2
4
1.00
1.00
1.60
1.64
2.51
2.28
Speedup (vs. 1 GPU)
0
1
2
3
1
2
4
Number of GPUs

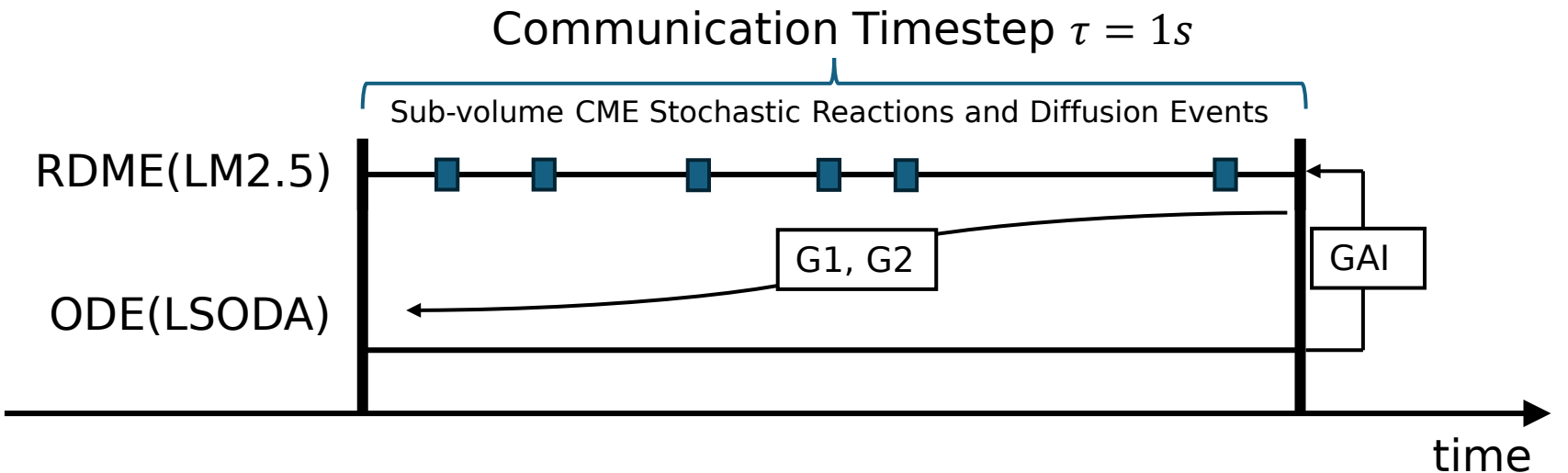
Communication Timestep $\tau = 1s$
Sub-volume CME Stochastic Reactions and Diffusion Events
RDME(LM2.5)
ODE(LSODA)
G1, G2
GAI
time

(a) G2 gene in activated state

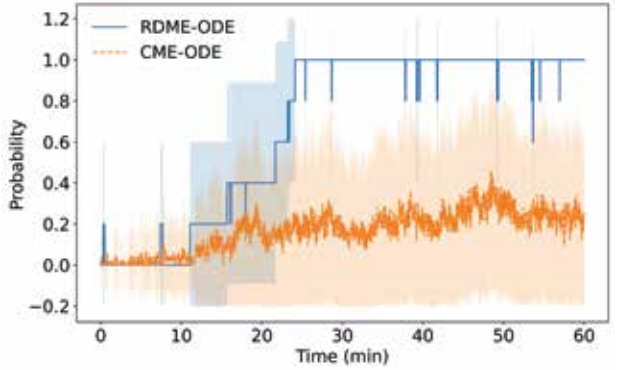

(b) mRNA for transporter G2

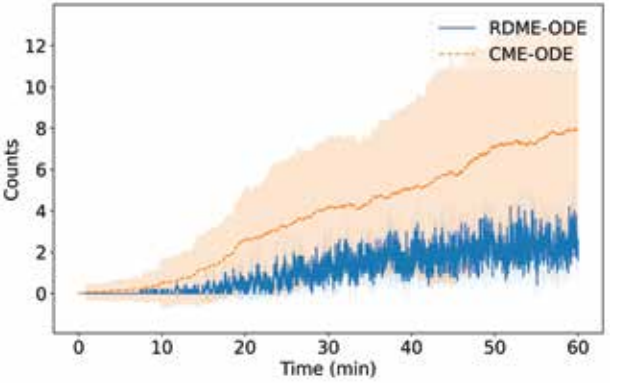

(c) Galactose transporter G2

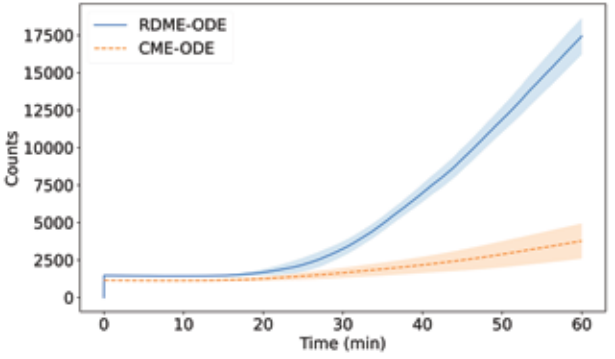

(d) Intracellular galactose concentration

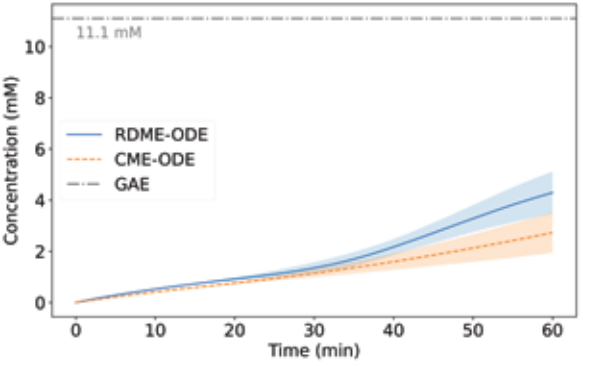

(e) G80d in nucleoplasm

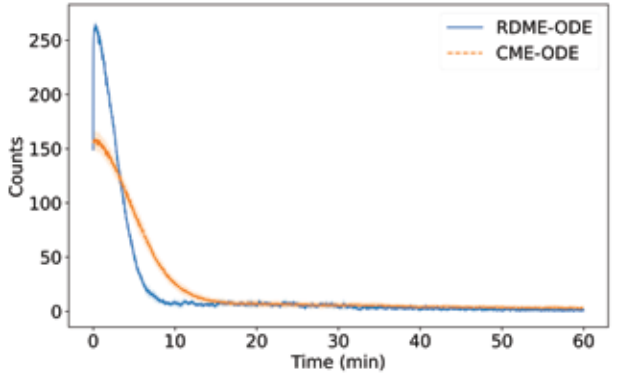

(f) G80dG3i

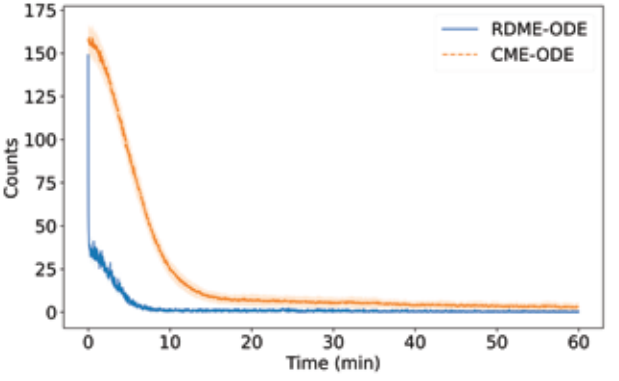

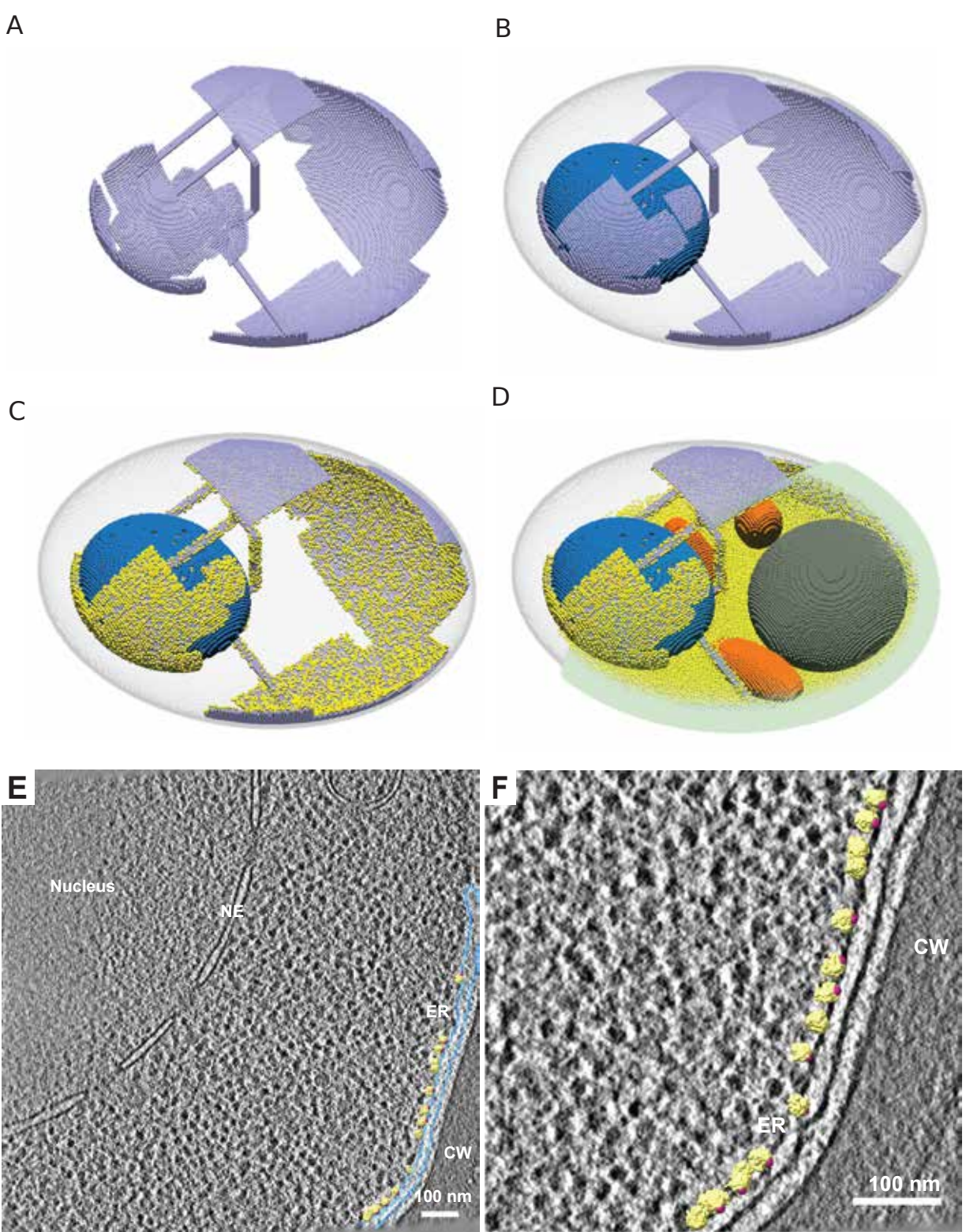
A
B
C
D
E
Nucleus
NE
ER
CW
100 nm
F
CW
ER
100 nm

(a) Free mRNA for transporter G2

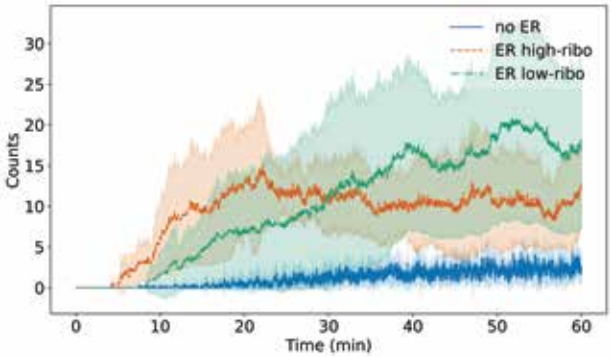

(b) Translating mRNA for transporter G2

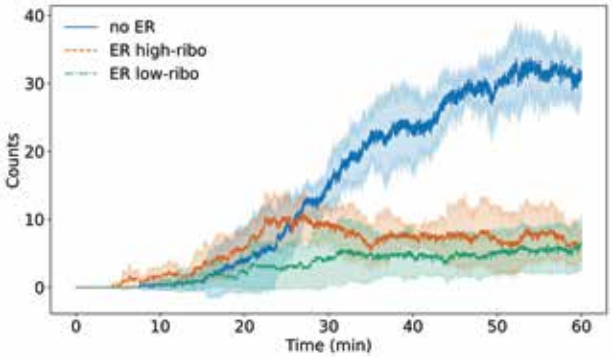

(c) Transporter G2 in cytoplasm(ER)

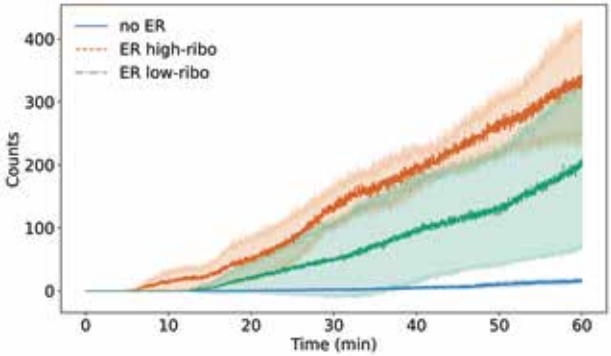

(d) Transporter G2 in plasma membrane

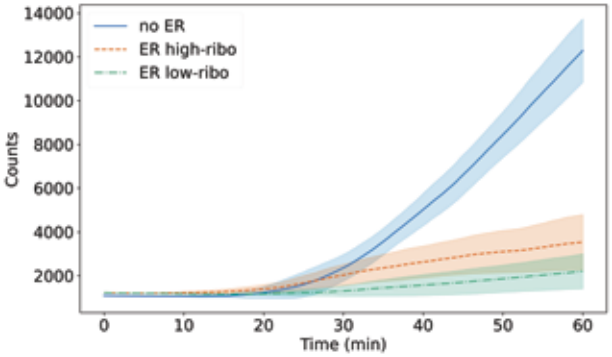

(e) Intracellular galactose concentration

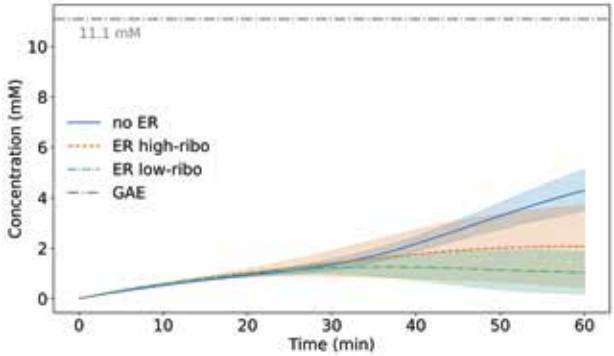

(f) Free ribosome

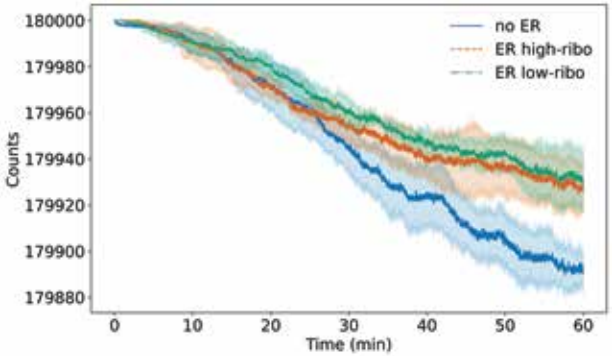

(a) Free mRNA for transporter G2

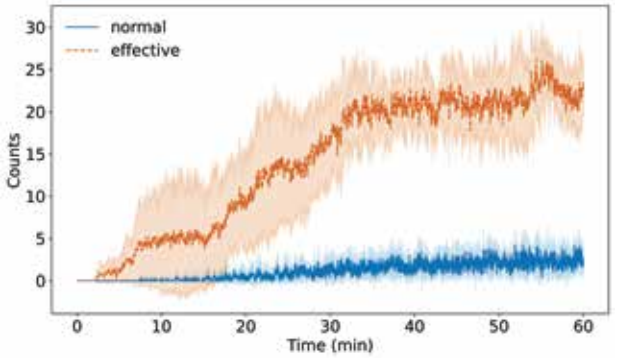

(b) Translating mRNA for transporter G2

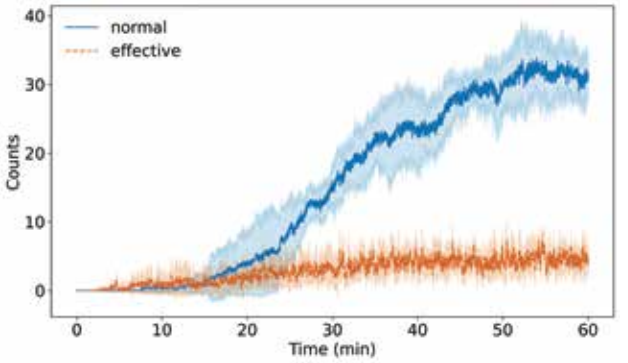

(c) Galactose transporter G2

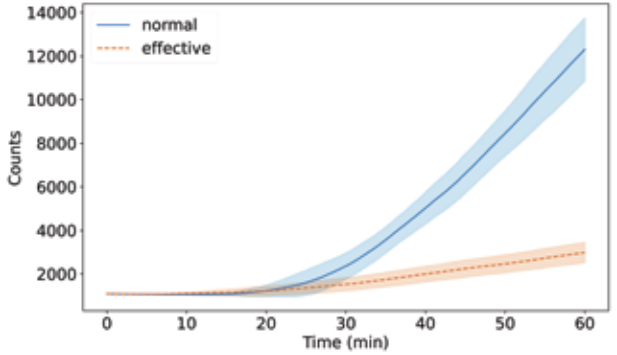

(d) Intracellular galactose concentration

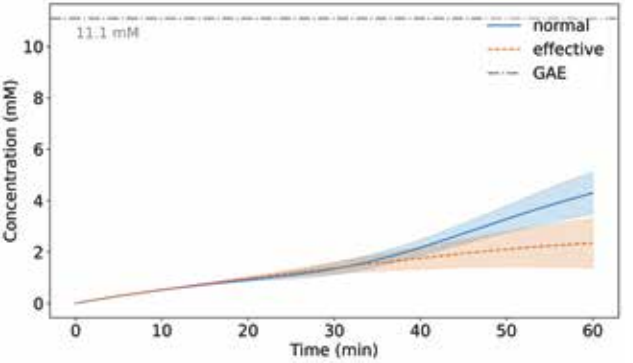

(e) Distance of translating ribosome to nucleus center

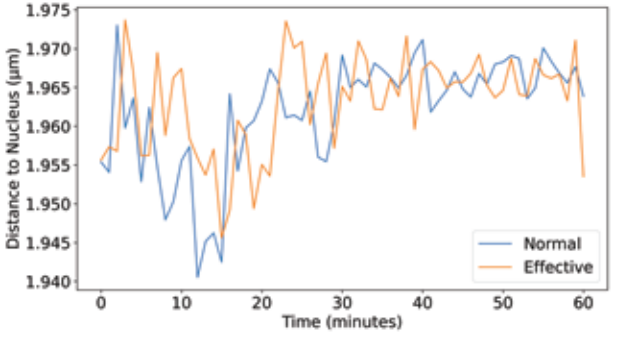
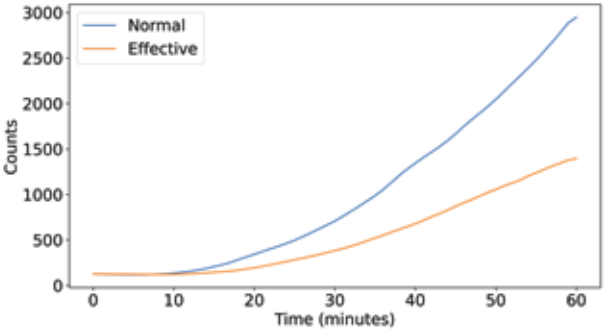
(f) Total translating ribosomes